Structure guided design and synthesis of furyl thiazolidinedione derivatives as inhibitors of GLUT 1 and GLUT 4, and evaluation of their anti-leukemic potential

Kalpana Tilekar, Neha Upadhyay, Jessica D. Hess, Lucasantiago Henze Macias, Piotr Mrowka, Renato J. Aguilera, Franz-Josef Meyer-Almes, Cristina V. Iancu, Jun-yong Choe, C.S. Ramaa

PII: S0223-5234(20)30575-4

DOI: https://doi.org/10.1016/j.ejmech.2020.112603

Reference: EJMECH 112603

To appear in: *European Journal of Medicinal Chemistry*

Received Date: 6 May 2020

Revised Date: 14 June 2020

Accepted Date: 18 June 2020

Please cite this article as: K. Tilekar, N. Upadhyay, J.D. Hess, L.H. Macias, P. Mrowka, R.J. Aguilera, F.-J. Meyer-Almes, C.V. Iancu, J.-y. Choe, C. Ramaa, Structure guided design and synthesis of furyl thiazolidinedione derivatives as inhibitors of GLUT 1 and GLUT 4, and evaluation of their anti-leukemic potential, *European Journal of Medicinal Chemistry*, https://doi.org/10.1016/j.ejmech.2020.112603.

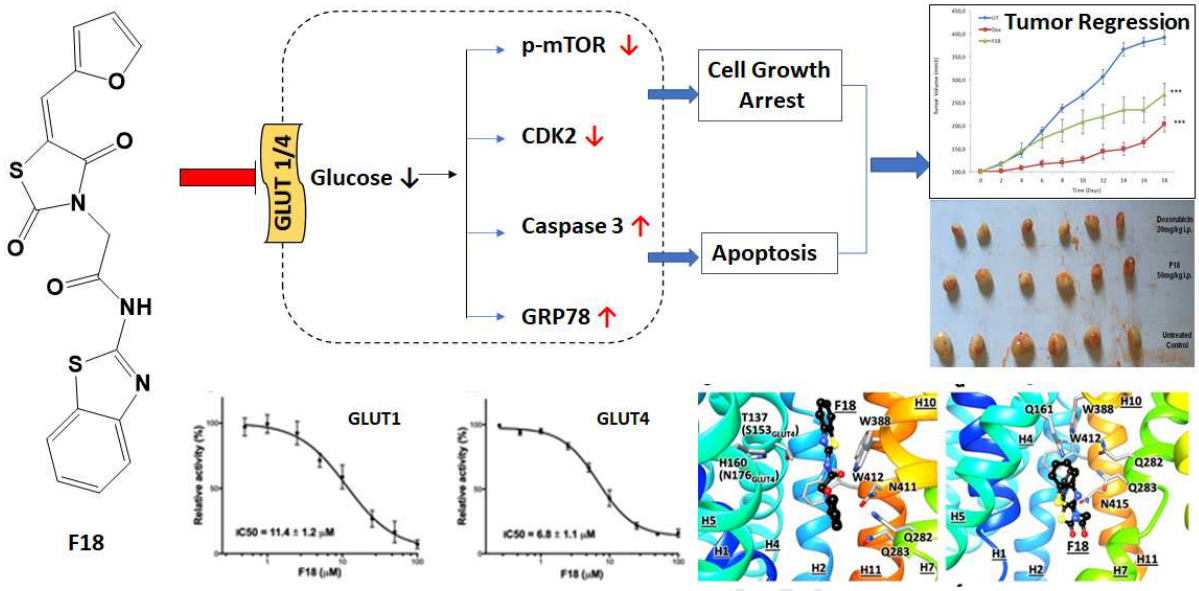

Structure guided design and synthesis of furyl thiazolidinedione derivatives as inhibitors of GLUT 1 and GLUT 4, and evaluation of their anti-leukemic potential.

Kalpana Tilekar[1], Neha Upadhyay[1], Jessica D. Hess[2], Lucasantiago Henze Macias[2], Piotr Mrowka[3], Renato J. Aguilera[2], Franz-Josef Meyer-Almes[4], Cristina V. Iancu[5], Jun-yong Choe[5,6*], C S Ramaa[1*],

[1]Department of Pharmaceutical Chemistry, Bharati Vidyapeeth's College of Pharmacy, Navi Mumbai, Maharashtra, India; [2]The Cytometry, Screening and Imaging Core Facility & Border Biomedical Research Center & Department of Biological Sciences, The University of Texas at El Paso, El Paso, Texas, USA; [3]Department of Biophysics and Human Physiology, Medical University of Warsaw, Chalubinskiego, Warsaw, Poland; [4]Department of Chemical Engineering and Biotechnology, University of Applied Sciences, Darmstadt, Germany; [5]East Carolina Diabetes and Obesity Institute, Department of Chemistry, East Carolina University, Greenville, North Carolina, USA; [6]Department of Biochemistry and Molecular Biology, The Chicago Medical School, Rosalind Franklin University of Medicine and Science, North Chicago, Illinois, USA.

Corresponding Authors

1. Dr C S Ramaa
Email: sinharamaa@yahoo.in

2. Jun-yong Choe
Email: choej18@ecu.edu

Abstract

Cancer cells increase their glucose uptake and glycolytic activity to meet the high energy requirements of proliferation. Glucose transporters (GLUTs), which facilitate the transport of glucose and related hexoses across the cell membrane, play a vital role in tumor cell survival and are overexpressed in various cancers. GLUT1, the most overexpressed GLUT in many cancers, is emerging as a promising anti-cancer target. To develop GLUT1 inhibitors, we rationally designed, synthesized, structurally characterized, and biologically evaluated *in-vitro* and *in-vivo* a novel series of furyl-2-methylene thiazolidinediones (TZDs). Among 25 TZDs tested, F18 and F19 inhibited GLUT1 most potently (IC_{50} 11.4 and 14.7 µM, respectively). F18 was equally selective for GLUT4 (IC_{50} 6.8 µM), while F19 was specific for GLUT1 (IC_{50} 152 µM in GLUT4). *In-silico* ligand docking studies showed that F18 interacted with conserved residues in GLUT1 and GLUT4, while F19 had slightly different interactions with the transporters. In *in-vitro* antiproliferative screening of leukemic/lymphoid cells, F18 was most lethal to CEM cells (CC_{50} of 1.7 µM). Flow cytometry analysis indicated that F18 arrested cell cycle growth in the subG0-G1 phase and lead to cell death due to necrosis and apoptosis. Western blot analysis exhibited alterations in cell signaling proteins, consistent with cell growth arrest and death. *In-vivo* xenograft study in a CEM model showed that F18 impaired tumor growth significantly.

Keywords Antiproliferative; Thiazolidinedione (TZD); Furan; Leukemia; Cytotoxicity; GLUT1, GLUT4; GLUT5; Inhibitor specificity

1. Introduction

A major challenge of cancer research is to identify target therapies that kill cancer cells while sparing normal ones. To keep pace with the rapid rate of proliferation and high energy requirement, tumor cells significantly increase their glucose dependence and metabolism[1–3]. Interestingly, cancer cells can shift their metabolism from aerobic oxidation to anaerobic glycolysis, irrespective of the oxygen levels. A direct consequence of this metabolic reprogramming is lower ATP production, leading to an increase in facilitative glucose transporters (GLUT, gene family SLC2) on the membrane surface[4]. Since GLUTs are upregulated in many cancer cell types, including leukemia[5,6], they provide a selective mechanism to kill tumor cells.

The human GLUT family has 14 members, which vary in substrate affinity and specificity, tissue localization and expression level[7–9]. For instance, GLUT1, 3, 4, 8, and 12 transport glucose, GLUT5 only transports fructose, GLUT2, 7, 9, and 11 transport both glucose and fructose, GLUT13 transports myo-inositol. Literature also reveals a correlation between inhibition of GLUTs and cancer suppression[10–13]. Given the number of GLUTs and their involvement in various types of cancers, the process is still very complex and hence the need for GLUT specific ligands[14].

Leukemia is a cancer of the bone marrow, a dynamic tissue consisting of different types of cells, interdependent for their proper functioning, growth, and survival. Since leukemic cells are rapidly growing, they exhibit high glycolytic activity. Several mutational changes, such as those in IDH1/2, have also been found in leukemia[15]. The high glycolytic activity, along with mutations, leads to microenvironment modifications that can alter the support capacity of stromal cells for normal blood-forming cells. The development of therapeutic agents that can reduce the glycolytic rate directly or indirectly in leukemic cells is expected to both control leukemic cell proliferation and also reverse changes in other cells within the bone marrow, returning them to normal hematopoiesis. Several reports indicate overexpression of GLUT1 and GLUT4 in various types of leukemia[16–18]. Fasentin binds directly to GLUT1 inhibiting glucose uptake of U-937 leukemia cells[19]. Nilotinib and imatinib, inhibitors of a tyrosine kinase, downregulate GLUT4 in chronic myeloid leukemia (CML)[20,21]. IL-3 stimulation is involved in the translocation of glucose transporter protein (GLUT1) to the cell surface in CML cells[22]. Small molecules have been found to inhibit GLUTs in acute myeloid leukemia (AML) cells, HL60 cells, and T-Cell lymphomas[17,23].

Several natural and synthetic inhibitors of the GLUT members have been reported[24–28], including Thiazolidinediones (TZD)[29,30]. TZD scaffold containing antidiabetic agents such as pioglitazone(PG), ciglitazone(CG) and troglitazone(TG) which are PPAR-γ agonists, exhibits moderate antiproliferative effects[31,32], but their usage was limited due to mounting evidences on side effects and toxicity of these drugs, which were attributed to the full agonistic activity at binding sit of PPARγ[33,34]. Thus, TZDs devoid of PPAR- γ agonistic activity retaining antiproliferative effects or exhibiting PPAR-γ independent antitumor effects, came in limelight. Recent studies of PPAR- γ inactive analogs of Ciglitazone (CG), Δ2CG, proved ability to mimic glucose starvation through the inhibition of glucose uptake[35]. Thus, TZD analogs possess the capacity to create glucose deficiency state in cancer cells and can act as energy restriction mimetics to achieve antitumor effects[36,37]. Interestingly, a couple of compounds possessing the TZD scaffold have been reported as dual PPARγ and GLUT4 activators of their protein expression (mRNA level), and found to have therapeutic applications as anti-diabetic agents[38,39]. Close observation of their structures reveals that the TZD ring location may determine the GLUT activity of the compound: activator of GLUT expression or GLUT inhibitor. Thus, we hypothesized that when the TZD ring is at one end of the molecule, the compounds exhibit GLUT upregulation, whereas placing it in the center (**Fig. 1**., Compound 2)[29] of the molecule leads to GLUT inhibitory potential. For more than a decade, we have been working on TZD scaffold modifications to achieve partial PPARγ agonistic[40,41], anti-angiogenic[42], and HDAC inhibitory activity[43,44]. In the current work, we have designed a novel series of TZD derivatives targeting GLUT1 based on insights obtained from the literature regarding desirable structural features for GLUT inhibition, and our knowledge of structure-based drug discovery (SBDD).

2. Results and Discussion

2.1. Designing aspects of Novel series of compounds F1-F25.

Not much literature is available about the fingerprints of structural features needed to develop inhibitors for GLUTs. Also, only a few crystal structures of human GLUTs liganded with inhibitors are available[45]. Some TZD-containing molecules are energy restriction mimetic agents, which selectively inhibit GLUT1[29,30,36]. A US patent by Chen. *et al*. have described novel TZD-based GLUT1 inhibitors with an IC_{50} value of 2 μM[29]. Our work has also been focused for more than a decade on TZD-based antiproliferative agents in anticancer drug discovery. We noticed the structural similarity of some of our previously reported TZDs (**3**)[46] (**Fig. 1**) with the commercially available GLUT1 inhibitor, Fasentin (**1**) [19] (GLUT1 IC_{50} =10 μM), and with a TZD molecule (**2**) reported by chen. *et al*.[29], which induced anticancer effects by inhibiting GLUT1. Therefore, we decided to explore TZD-based agents for GLUT1 inhibition.

Intriguingly, the above two classes of GLUT1 inhibitors and our previous TZD derivatives share the following pharmacophoric features:

a. Aryl acetyl amido (Ar-NH-CO-CH_2) functionality as present in Fasentin (**1**), and

b. 5-benzylidene-2,4-TZD scaffold similar to the compound **2**[29] molecule reported by Chen. *et al*

Thus, after carefully analyzing all three structures, we designed a novel series of potential GLUT1 inhibitors by modifying our previously reported TZDs to meet the structural requirements for GLUT1 inhibitory activity (**Fig. 1**). We kept the TZD ring in the middle of the molecule, as in the structures of GLUT inhibitors reported by Chen. *et al.*[29], since having it at the compound terminus may lead to GLUT upregulation[38,39]

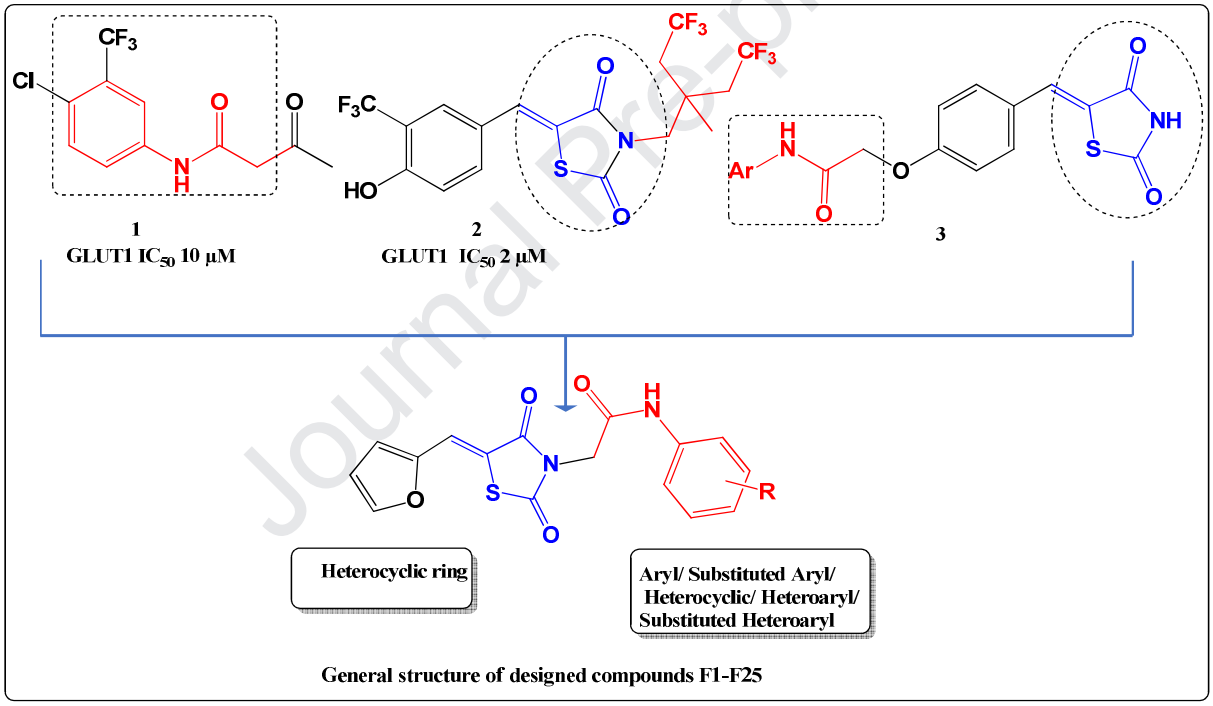

Figure 1. Designing a novel series of GLUT1 inhibitors. F1-F25 compounds were designed to incorporate features from two potent GLUT1 inhibitors, shared with our previously reported TZD-based antiproliferative series[46]: the aryl acetyl amido moiety (red) and the 5-benzylidene-2,4-TZD scaffold (blue).

3.2 Chemistry

Figure 2 outlines the synthetic pathway for the target compounds **F1-F25**. Their construction involved the synthesis of 5-(furan-2-ylmethylene) thiazolidine-2,4-dione, **5**, by refluxing furfuraldehyde, **3**, with 2,4-TZD, **4**, in the presence of acetic acid and a catalytic amount of sodium acetate. Compound **5,** on further treatment with ethanolic KOH, yielded potassium salt **6**, which was a common intermediate for all the target compounds. Both **5** and **6** were obtained in good yield. Compounds **2a-2y** resulted from N-chloroacetylation of various aromatic and heteroaromatic amines **(1a-1y),** using a weak base like K_2CO_3 in organic solvents such as dichloromethane (DCM). The final step involved the condensation between **2a-2y** and **6** in acetone to produce the target compounds **F1-F25.** The reactions were monitored for completion by thin layer chromatography. The structures of newly synthesized compounds were confirmed spectrally by ^{1}H NMR,^{13}C NMR, FTIR, and mass spectrometry (Supplementary Data).

FT-IR spectra of synthesized derivatives displayed characteristic absorption in the following domains: 3340-3166 cm^{-1} corresponding to $NH_{(s)}$ vibration of the amide group; 1687-1660 cm^{-1} corresponding to $C=O_{(s)}$ of the amide group, and 1080-1120 and 1200-1280 cm^{-1} corresponding to $C\text{-}O\text{-}C_{(s)}$ ether linkage of the furan ring.

Proton NMR spectra of **F1-F25** compounds showed a characteristic singlet of -NH of amide linkage in the region of δ=10.01-12.87 ppm. A characteristic singlet of furylidene -C=CH- was observed in the region of δ= 8.00-8.10 ppm for intermediates **5** and **6,** and final compounds **F1-F25**. The singlet of the two protons from methylene-CH_2 was observed at δ= 4.40-4.80 ppm, confirming the formation of the target compounds by condensation of **2a-2y** and **6**. The spectra also showed various peaks in the aromatic and aliphatic regions corresponding to the protons of variously substituted aromatic and heteroaromatic groups attached to the N atom of the amide linkage. Peaks of the furan ring appeared in the aromatic region at δ= 6.50-8.00 ppm.

Furthermore, ^{13}C NMR spectra of **F1-F25** compounds elicited characteristic peaks of carbonyl carbon, C=O, at δ=162-169 ppm, and of linker -CH_2 at δ=43-45 ppm. Furylidene carbon-C=CH- was found at δ= 147-148 ppm. They also had three peaks at δ=113-114, 115-118, and 149-150 ppm corresponding to the four carbon atoms of the furan ring. Various other peaks corresponding to carbon atoms of aromatic or heteroaromatic substitution at the N atom of the amide linkage were also observed.

The mass spectrum was recorded for both positive and negative ionization. There was extensive ionization in positive scanning, but in negative scanning, the characteristic [M-H^+] peak was observed at 40-100% intensity for all the compounds.

Details of the synthesis procedure and additional spectral observations are presented in Materials and Methods and Supplementary Data.

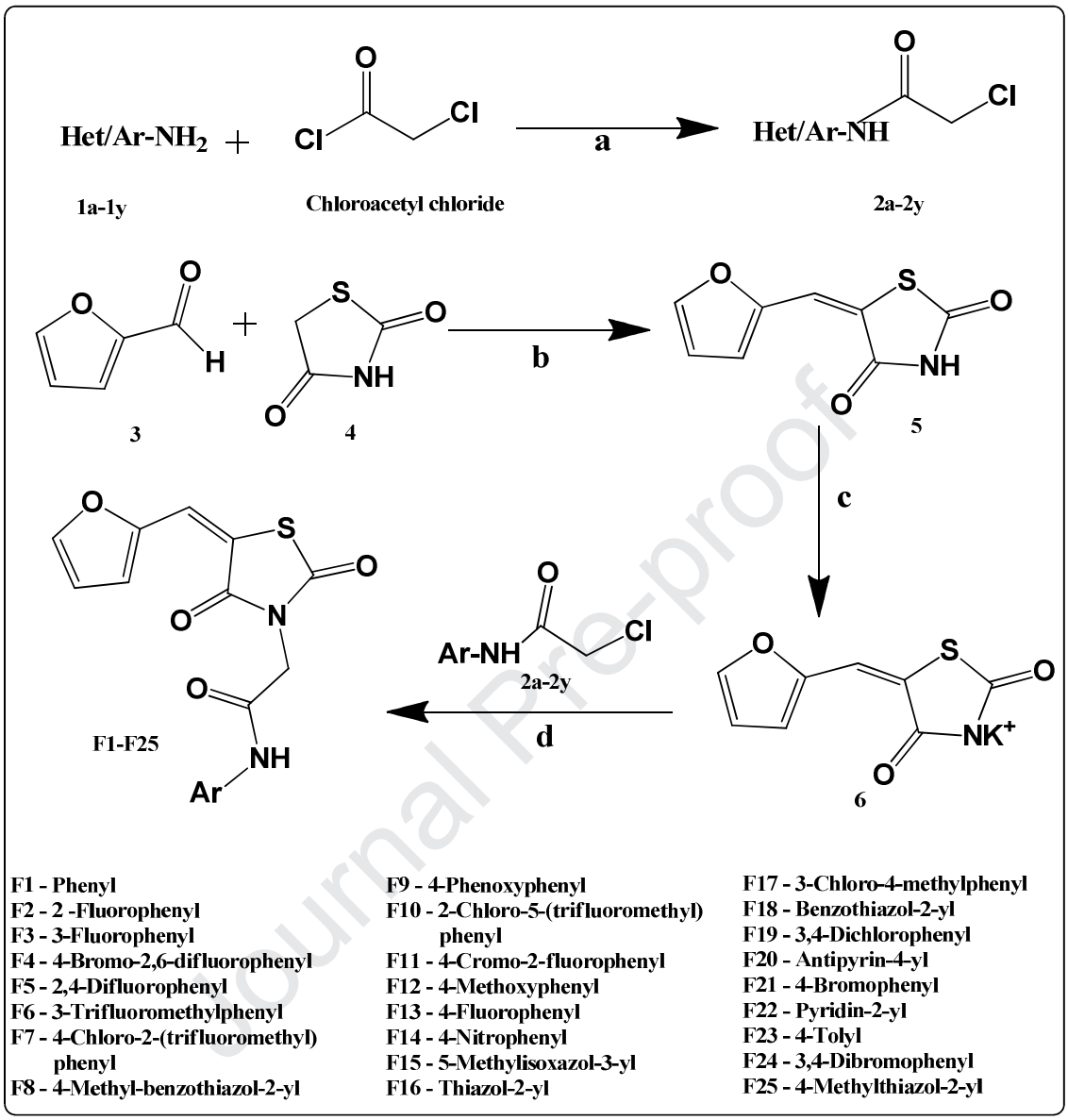

Figure 2. Synthetic route for the synthesis of intermediates and F1-F25. a) K_2CO_3, DCM, 24 hrs; b) AcOH, Sodium acetate, reflux 5 hrs; c) EtOH, KOH, reflux 3 hrs; d) Acetone, reflux 6 hrs. 'Het' and 'Ar' are abbreviations for heteroaromatic and aromatic, respectively. The specific aromatic moiety (Ar) in the final product is defined for each compound.

2.3. Screening for transport activity inhibition of GLUT1, GLUT4, and GLUT5.

To assay the transport activity and determine the effect of designed compounds on a singular GLUT, we used GLUT-specific assay systems: hexose transporter deficient yeast cells (*hxt*^{0}) expressing a particular human GLUT[47]. In *hxt*^{0} strains, yeast cell growth in hexose-based media relies solely on the transport activity of the expressing human GLUT for bringing the

carbon source into cells. Thus, GLUT transport activity is determined as the C^{14}-hexose uptake into whole cells[47]. The primary inhibition screening was carried out at 100 µM compound concentration on three glucose transporters: GLUT1, GLUT4, and GLUT5. For compounds that decreased the relative transport activity by 50% or more, inhibitor concentration was varied in the assay from 0.1 to 100 µM to determine inhibitor IC_{50}. In the primary screen, none of the tested compounds inhibited GLUT5 significantly, but the compounds **F8**, **F18**, and **F19** decreased the relative activity of GLUT1 and GLUT4 by at least 50% (**Fig. 3a-c**). **F8** was a weak inhibitor (**Fig. 3d, g;** IC_{50} 72 ± 3 µM and 123.3 ± 1.5 µM for GLUT1 and GLUT4, respectively). **F18** inhibited both GLUT1 and GLUT4 similarly, with IC_{50} values 11.4 ± 1.2 µM and 6.8 ± 1.1 µM, respectively (**Fig. 3e, h**). **F19** was more specific for GLUT1; its IC_{50} for GLUT1 inhibition (IC_{50} 14.7 ± 1.2 µM) was approximately ten times lower than that for GLUT4 (IC_{50}=152.3 ± 1.5 µM) (**Fig. 3f, i**). Nevertheless, **F19** was less efficacious than **F18** in inhibiting GLUT1; at 100 µM **F19** concentration GLUT1 retained ~ 30% of its relative activity, while the same concentration of **F18** inhibited GLUT1 almost completely (**Fig. 3e, f**). Thus, with experimental proof of GLUT1 and GLUT4 inhibition, our observation of differentiating TZD-containing analogs as activators of GLUT protein level or GLUT transport activity inhibitors, based on the position of the TZD ring terminally or centrally, may serve as a critical milestone in the discovery of TZD analogs as GLUT modulating agents and their application as antidiabetic and anticancer agents.

We had designed the molecules to target GLUT1 but found that **F18** and **F19** inhibited the activity of both GLUT1 and GLUT4, though with different affinities and specificities. Nevertheless, neither **F18** nor **F19** affected the transport activity of GLUT5. Based on sequence homology, GLUTs are divided into three classes; GLUT1 and GLUT4 belong to class I, GLUT5 to class II [48]. While both **F18** and **F19** seem to distinguish between class I and class II GLUTs, **F19** also discriminates between GLUT1 and GLUT4, making **F19** a promising starting point for the design of future GLUT1-specific probes.

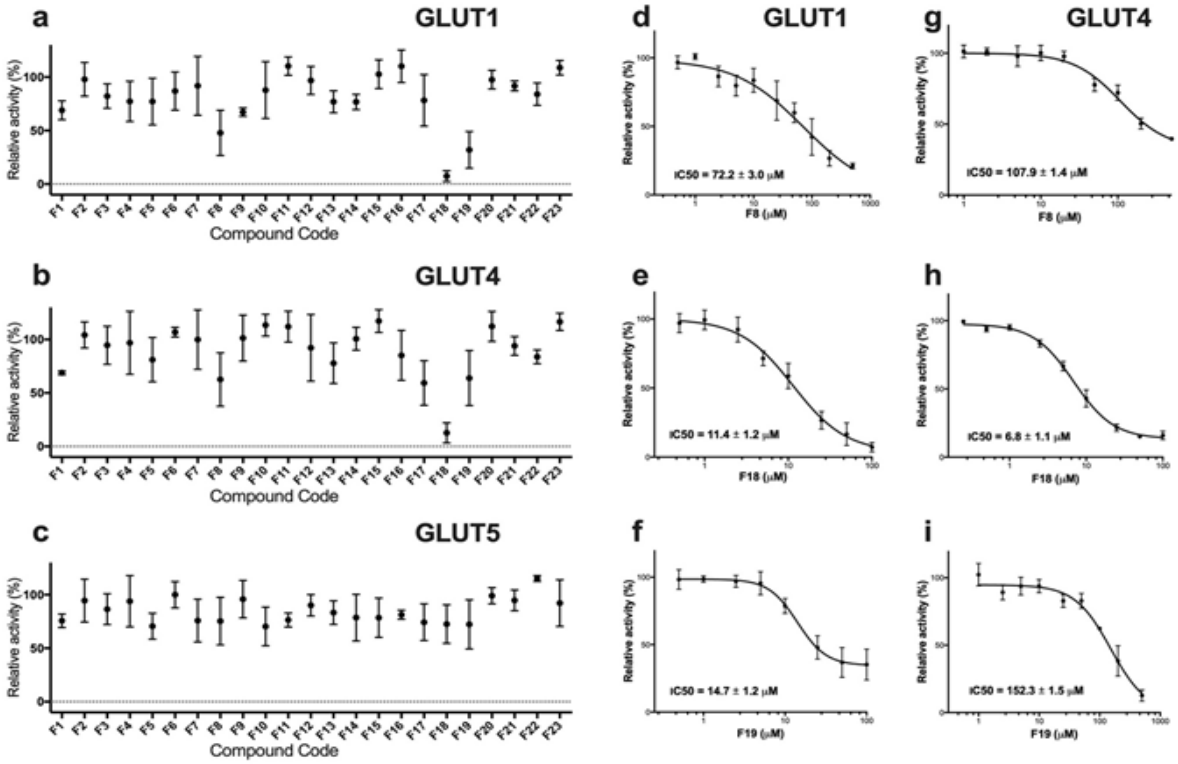

Figure 3. Screening of F1-F23 for inhibition of the transport activity by GLUT1, GLUT4 and GLUT5. Relative transport activity of GLUT1 (a), GLUT4 (b) and GLUT5 (c) in the presence of 100 μM concentration of **F1-F23**. Dose response curve of GLUT1 for **F8** (d), **F18** (e), and **F19** (f). Dose response curve of GLUT4 for **F8** (g), **F18** (h), and **F19** (i). Error bars represent standard deviation from three independent measurements. Transport activity was determined in *hxt*^{0} yeast cells expressing a single GLUT. Transport assay was initiated by the addition of 5 mM C^{14}- glucose for GLUT1 or GLUT4 or 10 mM C^{14}-fructose for GLUT5 and stopped after 10 minutes (see Materials and Methods for details).

2.4. Ligand docking studies.

Consistent with the alternating transport mechanism of the major facilitator superfamily (MFS) proteins, GLUTs have two major states for their substrate cavity: inward-facing (open towards cytoplasm) and outward-facing (open towards the extracellular space); these states have been captured in the crystal structures of GLUTs and their homologs[49]. Mutagenesis, functional, and structural data have established the location of the substrate binding site and the residues essential for substrate binding. **Fig. 4** shows the ligand docking of **F18** and **F19** to the inward-facing and outward-facing conformations of GLUT1. **F18** docks to the substrate binding site formed by residues Q282, Q283, W388, W412, and others, in both the inward- and outward-facing conformations of GLUT1. However, **F19** docks to the substrate binding site only in the

inward-facing conformation. In GLUT1 and GLUT4, the residues forming the substrate binding site in the outward-facing conformation are conserved but those forming the inward-facing conformation have two differences: $T137_{GLUT1}$ vs. $S153_{GLUT4}$ and $H160_{GLUT1}$ vs. $N176_{GLUT4}$ (**Supplementary Data, Table S3**). In the inward-facing conformation, **F19** docks close to H160 (4 Å between Cl of **F19** and the imidazole of H160), which is N176 in GLUT4. Interestingly, H160 is adjacent to the highly conserved Q161[50] and varies in all other GLUTs, except for GLUT2 (**Supplementary Data, Table S3**). On the other hand, **F18** does not interact with either T137 or H160. The validation of modeled structures was done by docking n-nonyl-β-D-glucopyranoside to GLUT1 crystal structure (PDB ID 4PYP) (**Supplementary Data, Fig. S1**).

Thus, **F18** can bind to both the inward- and outward-facing conformations of GLUT1 and GLUT4, interacting with conserved residues in these transporters, whereas **F19** binds only to the inward-facing conformation of the transporters, and may interact differently with GLUT1 and GLUT4. The increased stabilization of the chlorine charge by the pyrrole nitrogen of H160 compared to the carboxamide of N176 may account for the 10-fold difference in the IC_{50} of **F19** for GLUT1 and GLUT4, and suggests a way to increase ligand specificity in GLUT1: optimize ligand interactions with H160 versus its substitution in GLUT4 or other GLUTs, especially given the low conservation of this residue in other GLUTs. **Supplementary Data, Fig. S2** shows the two-dimensional representation of GLUT1 interactions with **F18** or **F19** generated with MOE (https://www.chemcomp.com) ligand interaction function.

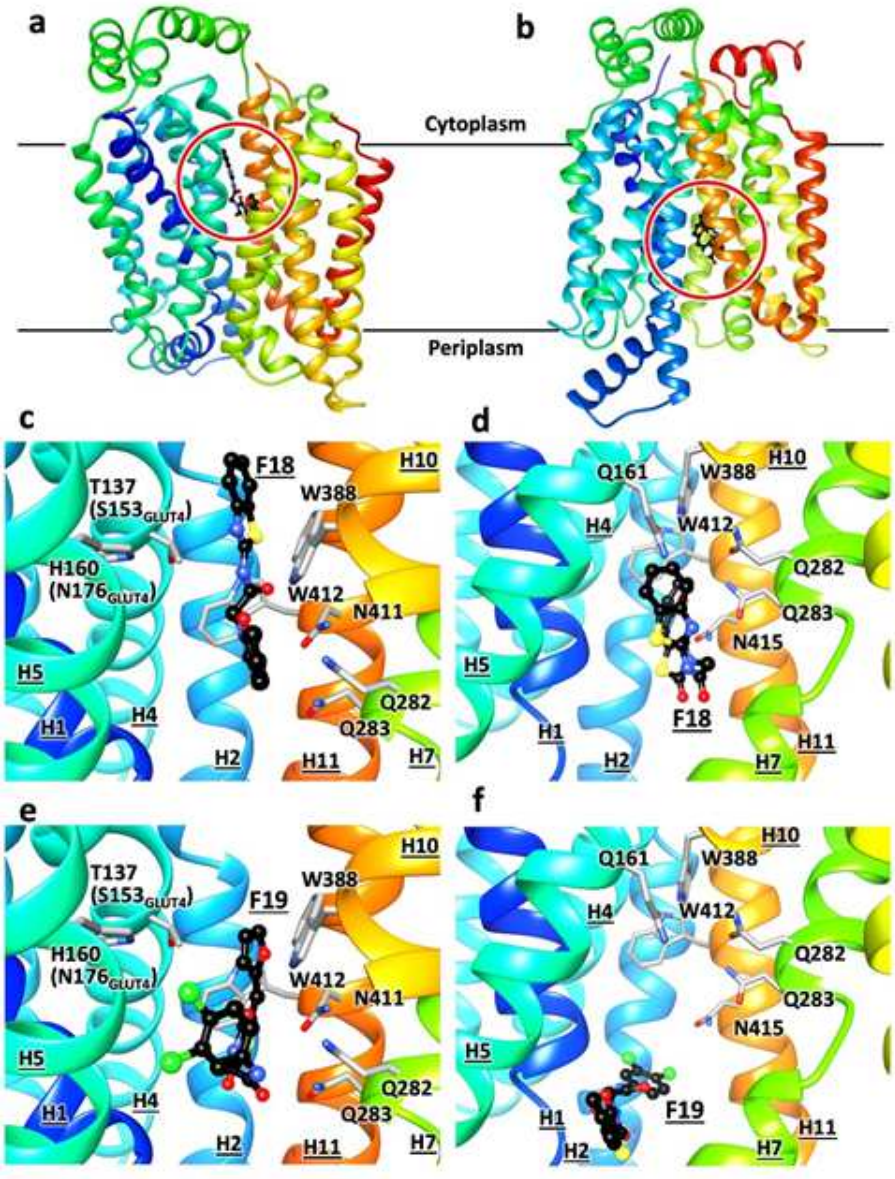

Figure 4. Docking of F18 and F19 to GLUT1. Inward- (a) and outward-facing (b) conformations of GLUT1. Red circles show the substrate binding site. **F18** and **F19** are shown as ball and stick model. Close-up view of **F18** docking to the inward- (c) and outward-facing (d) conformations of GLUT1. Close-up view of **F19** docking to the inward- (e) and outward-facing (f) conformations of GLUT1. **F19** docks away from the substrate binding site in the outward-facing conformation and does not have significant interactions with protein residues. Labeled GLUT1 residues Q161, Q282, Q283, W388, N411, and W412 are conserved in GLUT4; however, T137 and H160 are S153 and N176 in GLUT4, respectively. H1, H2, H4, H5, H7, H10 and H11 indicate the transmembrane helices surrounding the substrate cavity. The figure was drawn using UCSF Chimera version 1.12 (http://rbvi.ucsf.edu/chimera/).

2.5. Prediction of physicochemical, pharmacokinetic, and ADME properties with SwissADME.

To predict the physicochemical and pharmacokinetic properties of the compounds, *in silico* calculations were performed using the SwissADME server[51,52] (**Supplementary data, Table S1)**. Results showed that the molecular weights of **F1-F25** ranged between 328.34 and 486.13 g/mol, octanol–water partition coefficient ilogP[51] varied from 1.97 to 3.20, topological polar surface area (TPSA) was between 104.92 and 150.74 $Å^2$. The number of hydrogen bond acceptors was <10, and of hydrogen bond donors was <5. Sixty percent of the compounds were predicted to be soluble, and the rest moderately soluble. The solubility of the latter could be mitigated using solubility enhancement techniques such as salt formation. Eighty percent of the compounds exhibited high gastrointestinal tract (GIT) absorption. All the compounds were predicted not to penetrate the blood–brain barrier (BBA), indicating no CNS adverse effect. Also, compounds were predicted not to be substrates for P□glycoprotein (P□gp). P-gp, present in different organs, acts as an efflux transporter and pumps xenobiotics out of the cells leading to increased clearance of drugs[53]. All 25 compounds had a bioavailability score of 0.55 and fulfilled the drug-likeness as indicted by Lipinski's rule of five[54], Veber's rule[55], Ghose filter[56], Egan rule[57] and Muegge's filter[58], except for molecular weight in some cases.

The bioavailability radar plot depicts the predicted oral bioavailability, and its pink zone shows the ideal zone for lead-like molecules. This optimum radar zone appraises six physicochemical properties: size, polarity, lipophilicity, solubility, saturation, and flexibility. **Supplementary Data, Fig. S3** shows the bioavailability radar plot of compounds **F18** and **F19**. All compounds **F1-F25** were in the pink zone, with the degree of saturation slightly deviating out of the radar as the fraction of sp3 hybridized carbons was less than 0.25. For **F8**, **F14**, **F16**, **F18,** and **F25**, polarity slightly deviated out of the pink zone as TPSA was >140 $Å^2$. Thus, the results of the *in silico* ADME prediction analysis suggest that this series of compounds have favorable physicochemical and pharmacokinetic properties indicative of drug□likeness.

2.6. Cell viability assay of TZD derivatives.

To evaluate the cytotoxic potential of this compound series, we performed the Differential Nuclear Staining (DNS) assays after exposing human hematologic cancer cell lines to each compound, individually, for 48 hours. The DNS assay uses two fluorescent nuclear stains, Hoechst 33342 and Propidium iodide (PI), to selectively label living and dead cells[59]. In the initial high-throughput screening of all compounds, K-562, KCL-22, and CEM leukemia cells, and triple-negative breast cancer MDA-MB-231 cells were treated with 50 μM compound concentration. Each compound solubilized in DMSO at the desired concentration was directly added to cell-containing wells at a final concentration of 1% (v/v) DMSO. Out of 25 compounds,

seven induced considerable cell death (>50%) in one or more cancer cell lines (**Supplementary Data, Fig. S4**). These seven compounds were further assessed in a concentration range of 0.5-100 μM via a secondary DNS assay on all three leukemic cell lines to estimate their cytotoxic concentration 50% (CC_{50}) values (**Table 1**); CC_{50} indicates the concentration of a given compound needed to kill 50% of the cell population. CC_{50} values were estimated by linear interpolation of the two concentrations nearest 50% cell death. Except for **F18** and **F19**, all other compounds had moderate antiproliferative effects in all three leukemic cell lines tested with CC_{50} values in the mid-micromolar range in one or more leukemia cell lines. **F19** CC_{50} values were in the mid-micromolar range in the K-562 cell line. Interestingly, **F18** and **F19** demonstrated potent cytotoxicity at low-micromolar concentration toward CEM acute lymphoblastic leukemia cells (CC_{50} = 1.7 μM and 7.8 μM, respectively), but were less effective against K-562 and KCL-22 chronic myelogenous leukemia cell lines. CC_{50} value of **F18** in MDA-MB-231 was in mid-micromolar range (**Table 1**). Notably, except for **F18**, substantial dose-dependent crystallization was observed at concentrations over 50 μM. These crystals were roughly cell-sized but were easily excluded when quantifying cell death via IN Cell Analyzer software.

The cytotoxic effect of the two most active compounds, **F18** and **F19**, against non-cancerous human HS-27 fibroblasts was assessed after 48 hours of treatment with concentrations ranging from 1 to 100 μM. The CC_{50} value for **F18** was 44.0 ± 2.75 μM, while F19 elicited an average of just 27.32% cell death at 100 μM. When compared to the CC_{50} values of **F18** and **F19** against CEM leukemia cells, 1.7 μM and 7.8 μM respectively, these derivatives demonstrated significant cancer-selectivity. Selective cytotoxic index (SCI) values of **F18** and **F19** were calculated to indicate the capacity of these compounds to preferentially kill cancer cells in vitro. **F18** was highly selective toward CEM (CC_{50} 1.7 μM) with an SCI value of 25.8. F19 was also highly selective, with an SCI greater than 12.8. These findings suggest that **F18** and **F19** could be safe for normal cells at therapeutic dosage.

Table 1 Cytotoxic concentration 50% (CC_{50}) values of active F-series compounds in human cancerous and non-tumorigenic cell lines. CEM, K-562, and KCL-22 are leukemia cell lines, MB-231 is an abbreviation for MDA-MB-231**,** a triple-negative breast cancer cell line. HS-27 is a normal foreskin fibroblast cell line.

Cell Line	**CC_{50} (μM)[#]**						
	F7	**F8**	**F15**	**F18**	**F19**	**F21**	**F23**
CEM	79.9 ± 3.74	96.8 ± 0.61	>100	1.7 ± 0.03	7.8 ± 1.6	81 ± 1.12	102.1 ±0.16
K-562	>100	97.1 ± 0.5	98.6 ± 1.04	91.9 ± 2.61	43.3 ± 3.27	94 ± 1.28	>100
KCL-22	>100	97 ± 1.94	>100	15.3 ±	72.2 ±	98.2	>100

				2.53	1.63	±1.79	
MB-231	nd	nd	nd	45.1 ± 0.24	nd	nd	nd
HS-27	nd	nd	nd	44.0 ± 2.75	>100	nd	nd

[#]Values are reported as the mean ± the SD of 4 replicates per treatment. *nd - not determined.

2.7. HDAC enzyme activity assay.

We have reported an N-substituted TZD analog as an HDAC inhibitor in our earlier work[44], and current **F1-F25** series compounds are also N-substituted TZD derivatives. Even though the designing of the molecules is entirely different, to ascertain the selectivity of these compounds for GLUTs over HDACs, we undertook HDAC screening of **F1-F25** on two subtypes, HDAC4 and HDAC8. We selected these two isoforms as they possess high deacetylation activity and represent two different classes of HDAC, class1 (HDAC 8) and class II (HDAC4). The primary screening was performed with 50 µM of **F1-F25** (**Fig. 5, Supplementary Data-Table S4** and **Table S5)**. Only one compound, **F14,** produced a significant change in HDAC8 activity (residual enzyme activity: (17±3) %). The IC_{50} of **F14** was subsequently be determined to be 13 µM. However, **F14** did not inhibit GLUT1, 4, or 5, and **F25** was not evaluated for GLUT inhibition. All remaining compounds retained HDAC activity greater than 50% for HDAC8 and HDAC4, respectively, indicating that these derivatives may not interact with HDACs to such an extent to elicit therapeutic effect.

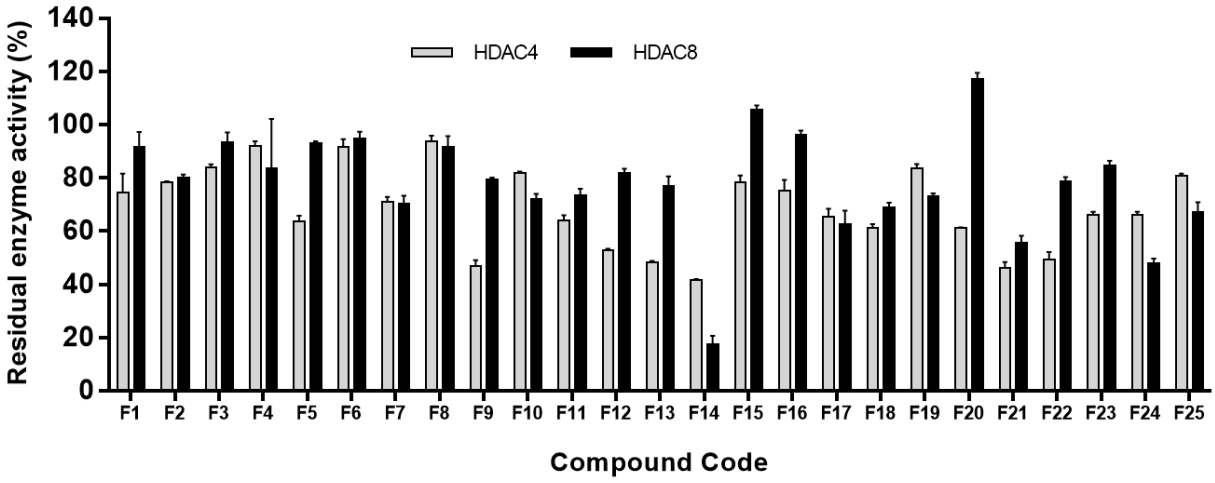

Figure 5. Histone Deacetylase (HDAC) activity assay. Percent relative activity of HDAC4 and HDAC8 after treatment with **F1-F25** at 50 µM concentration. Values were determined in triplicates and presented as Mean±SD.

2.8. Apoptosis studies

Apoptotic cell death of cells treated with GLUT inhibitors has been observed in various cancerous cells; it has been attributed to activation of caspase 8 and 3[60], sensitizing cells to FAS, a death receptor belonging to the TNF family[24]. GLUT1 inhibitors can decrease the levels of GLUT1, intracellular ATP, and glycolytic enzymes, leading to cell-cycle arrest, senescence, and necrosis through an increase in expression of AMPK, an ATP sensing enzyme, and decrease in cyclin E2[61]. OSU-CG5, a TZD derivative, has been shown to induce apoptosis through induction of ER stress[37]. Thus, the consequences of GLUT inhibition, which lead to anticancer effects, are the induction of apoptosis, necrosis, and cell cycle arrest. In agreement with these observations, our GLUT1/GLUT4 inhibitor, **F18**, exhibited apoptotic and necrotic cell death in lymphoid leukemic CEM cells (**Supplementary Data, Fig. S5)**.

To examine whether the cytotoxicity induced by **F18** is linked to apoptosis, we used CEM cells treated with annexin V-FITC/PI double staining and determined the rate of apoptosis by flow cytometry. Treatment of **F18** in CEM cells at its CC_{50} concentration caused an increase of cell population in the apoptotic region as compared to control (**Fig. 6b**). For **F18,** the percentage of apoptotic cells in the late and early apoptosis region was 55.87% and 1.38%, respectively. The percentage of live cells was only 26.14% compared with 92.15% of control (refer to **Supplementary Data** for cytograms, **Fig. S6)**. A considerable number of cells (16.60%) were observed in the necrotic region, in agreement with observations by Liu *et al.*, who have reported that WZB117, a GLUT1 inhibitor, induces cell-cycle arrest and necrosis as a consequence of GLUT1 inhibition[61]. Thus, our results suggest that compound **F18** can cause apoptotic death in the CEM cell line by induction of apoptosis and necrosis. This drug-induced cell death is, at least in part, attributable to apoptosis, as demonstrated by an increase in caspase 3 cleavage in response to compound **F18** (see below in western blotting section).

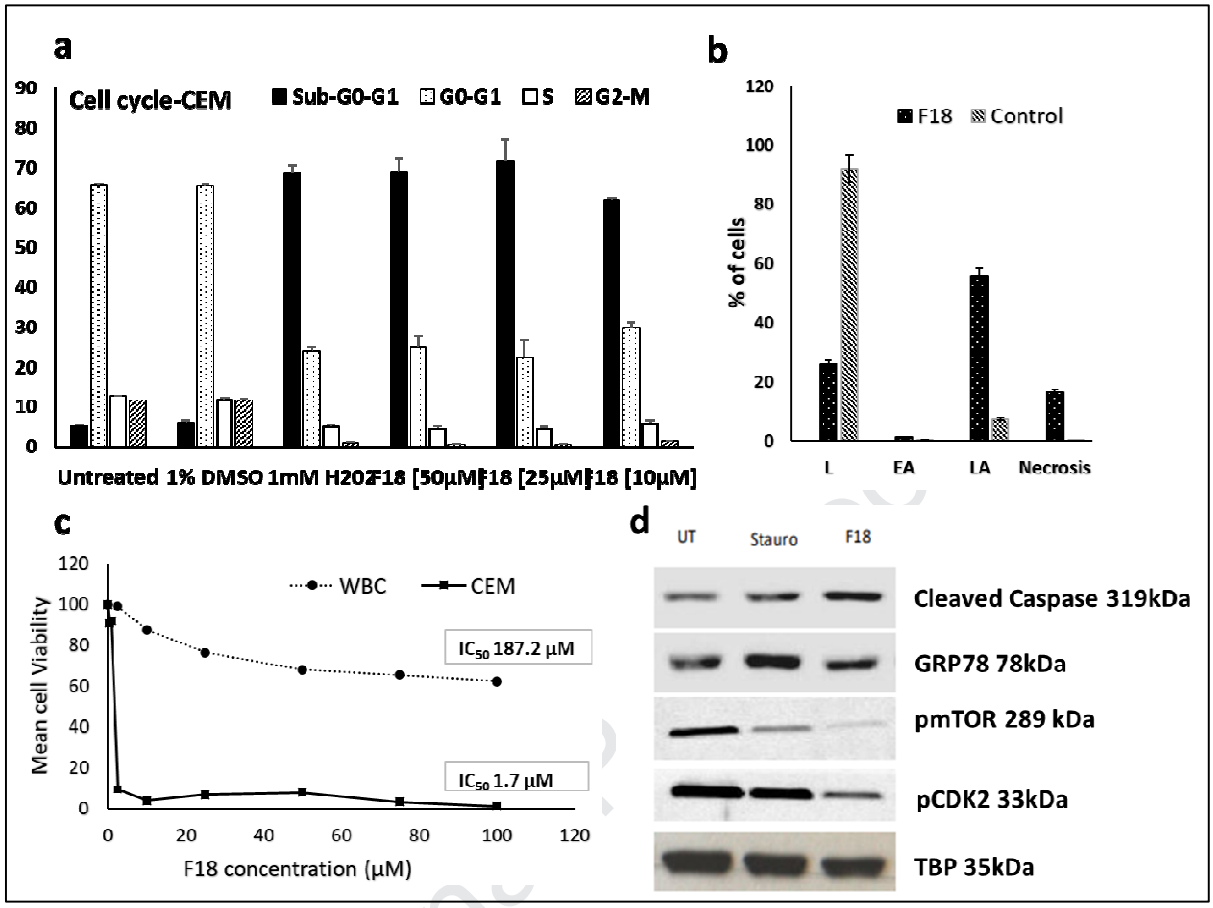

Figure 6. ***In vitro*** **cytotoxicity screening and** ***in vivo*** **impact of F18 on a CEM xenograft tumor model.** (a) Flow cytometry analysis of CEM cells treated with F18 (n=3, P = ≤ 0.001). Controls were: untreated cells, cells treated with 1% DMSO, or 1 mM hydrogen peroxide (H_2O_2). Concentrations for **F18** treatment were 10, 25 and 50 µM. (b) Graphical representation of apoptotic events of untreated and **F18**-treated CEM cells. L-Live cells, EA- Early apoptotic, LA-Late apoptotic. (n=3, P =≤ 0.001). (c) Dose response curves of **F18** in CEM cells (continuous line) and WBCs (dotted line); the mean cell viability is plotted versus increasing concentrations of **F18**. Human leukemic cell line CEM and normal WBC cells were treated with various **F18** concentrations for 48 hours. (d) Western blot analysis of markers associated with: apoptosis (Caspase 3), cell cycle regulation (p-mTOR and CDK2), and ER stress (GRP78) in **F18**-treated cells (F18) and controls (UT – untreated cells, Stauro - staurosporin positive control).

2.9. Cell cycle analysis

Cell cycle progression was assessed via a Beckman Coulter Gallios flow cytometer to investigate if compound **F18** perturbs this process. CEM cells were exposed to 50 µM, 25 µM, or 10 µM of **F18** for 72 hours, then permeabilized and stained in a single step with a NIM-DAPI reagent

(Beckman Coulter). The fluorescent signal of DAPI was then analyzed to quantify DNA content in each sample[62]. A dose-dependent increase in DNA fragmentation, as indicated by the sub G0/G1 population, was observed in cells treated with **F18 (Supplementary Data, Fig. S5)**. The G0/G1, S, and G2-M phases were also significantly disrupted in a dose-dependent manner (**Fig. 6a**). Treatment with **F18** caused cell cycle disruption, closely mirroring that of the hydrogen peroxide positive control and displaying arrest of the cell cycle in the sub G0/G1phase.

2.10. Western blotting

After identifying changes related to glucose transport activity, apoptosis, and changes in cell cycle regulation, Western blotting was performed to identify the consequences of the treatment with **F18** on cell signaling proteins such as p-mTOR, CDK2, GRP78 and Caspase 3. GLUT1 inhibitors can downregulate the levels of mTOR and Akt, phosphorylated enzymes involved in cell growth signaling pathway, and energy homeostasis[63–65]. Endoplasmic reticulum (ER) stress studies of GLUT inhibitors found increased levels of ER stress markers such as GRP78/BiP and PKR-like endoplasmic reticulum kinase (PERK)[66], indicating induction of ER stress leading to apoptosis. Phosphorylated retinoblastoma (pRb) regulates G1 arrest, and phosphorylation of pRb is controlled by the cyclin-dependent kinase (CDK)2/cyclin E2 complex. Thus, downregulation of CDK2 or cyclin E2 leads to decreased level of phosphorylated pRb and arrest of cells in early G1 phase[61,67–69]. The relationship between cell cycle progression and caspase 3 activation in leukemic cells has been demonstrated and found to be associated with G1 phase arrest. Activation of caspase 3 cleaves the substrate DNA triggering fragmentation leading to apoptosis[70].

In agreement with these observations, Western blot analysis of lysates from cells treated with 10 μM **F18** for 6 hours showed a decrease in levels of phosphorylated mTOR and CDK2 proteins, an increase in endoplasmic stress marker, GRP78, and activation of caspase 3 (**Fig. 6d**). Together, data revealed that after exposure to **F18**, cancer cells experienced a drop in glucose levels due to GLUT inhibition and maybe a concomitant decrease in some key glycolytic enzymes and metabolites like ATP and lactate[61]. This further leads to changes in key enzymes, particularly mTOR and CDK2. All these changes cause cell cycle arrest, accompanied by induction of ER stresses and caspase 3 activation, further inhibiting cancer cell growth. Thus, early G1 arrest, mediated by downregulation of CDK2 and phosphorylation of mTOR, induction of ER stress, DNA fragmentation by activation of caspase 3, and subsequent necrosis/apoptosis was the major mechanism underlying the inhibitory action of F18 on cancer cell growth.

2.11. F18 effect on the viability of non-transformed WBCs.

We evaluated the cytotoxic effects of **F18** on normal WBCs by MTT assay after treatment of WBCs with **F18**, at concentrations ranging from 2.5 to 100 μM, for 48 h (**Fig. 6c**). The IC_{50} value (187.2 μM) was 107 times greater than that for the CEM cell line (1.7 μM). More than 62%

of the WBCs were viable even after treatment with the highest concentration of F**18** (**Supplementary Table S2).** Hence, these findings suggest that **F18** could not be interfering much with the metabolic activities of normal blood cells and could be safer to them.

2.12. In-vivo effect of F18 on the CEM xenograft tumor.

To examine if **F18** has *in-vivo* anticancer activity in CEM cells, we established an *in-vivo* xenograft model with CEM cells. A total of 18 SCID mice were used, and tumors were generated using CEM cell lines. When the tumor reached palpable size, mice were randomly divided into three groups: the untreated group received the saline vehicle, the standard drug treated group received 20 mg/kg of doxorubicin, and the test drug group received 50 mg/kg of **F18** for 18 days (details in Supplementary Information). Tumor volume was measured every two days. Treatment with **F18** impaired the growth of tumors, as evidenced by the tumor growth curve (**Fig. 7a**) and tumor size (**Fig. 7b**). In the untreated group, all xenografts continued growing, and the volumes of the xenografts were approximately 1.5 and 2 times higher compared with those of xenografts from the doxorubicin and **F18** treated groups, respectively. Thus, **F18** exhibited potent *in-vivo* antitumor activity, which was comparable to doxorubicin but at a higher dose and far better than the untreated control. Moreover, throughout the experiment, no considerable weight loss or any other noticeable signs of toxicity were observed in any of the mice treated with **F18**.

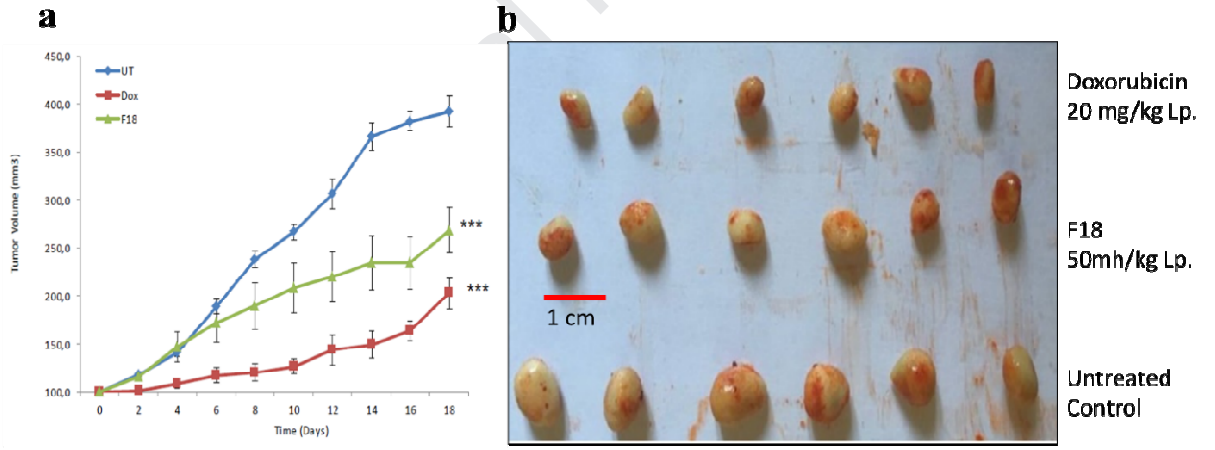

Figure 7. Tumor regression by F18 in CEM xenograft model. (a) Graph of tumor volume vs. time in CEM xenografts treated with doxorubicin 20 mg/kg i.p. (red), **F18** 50 mg/kg i.p. (green), and saline i.p. (blue). Error bars represent SEM n=6. $p<0.001$. (b) Excised tumor image of the animals treated with doxorubicin 20mg/kg i.p. , F18 50 mg/kg i.p. ,untreated saline i.p.

3. Conclusion

This series of furyl TZDs was designed for GLUT1 inhibition, wherein we found that two compounds, **F18** and **F19,** inhibited both GLUT1 and GLUT4. **F19** had higher selectivity for

GLUT1, and ligand docking analysis showed that **F19** could only bind to the inward-facing conformation of the transporters, with slightly different interactions in GLUT1 and GLUT4. **F18** inhibited potently and comparably both GLUT1 and GLUT4, as indicated by the IC_{50} values, consistent with the ligand docking analysis showing that **F18** had similar interactions with both transporters, irrespective of the transporter state (i.e., substrate cavity opened to either side of the membrane). The compound **F18** was taken further for *in-vitro* and *in-vivo* antiproliferative evaluation. It exhibited promising cytotoxic effects in the CEM cell line, in sub-micromolar range, and flow cytometric analysis indicated that **F18** arrested cell cycle growth in the sub G0-G1 phase and lead to cell death due to necrosis and apoptosis. On the other hand, normal cells withstood 100-fold higher **F18** concentrations than CEM cells, indicating that **F18**, besides its drug-likeness shown in the ADME analysis, may also be safe on non-cancerous cells. Western blot analysis data supported apoptosis and cell growth arrest in **F18**-treated cells, as evidenced by changes in the levels of proteins involved in cell growth signaling: downregulation of p-mTOR and CDK3, activation of caspase 3, and induction of ER stresses by increased levels of ER stress marker, GRP78. These changes suggest that GLUT inhibition could lead to cell growth inhibition and apoptosis (**Fig. 8**). **F18** demonstrated its antiproliferative effects in the *in-vivo* xenograft study too, wherein it impaired the growth of tumors much more effectively compared to untreated tumors. Thus, based on our observations, it appears that the beneficial anticancer effects of **F18** are due, at least in part, to inhibition of GLUT1 and GLUT4. **F19** also looks promising as it inhibits the growth of CEM cells at the sub-micromolar range and may exert beneficial effects if evaluated further. Furthermore, given the increased selectivity of **F19** for GLUT1, the interactions of **F19** with GLUT1, particularly involving residue H160, can be exploited in designing even more potent and specific GLUT1 inhibitors.

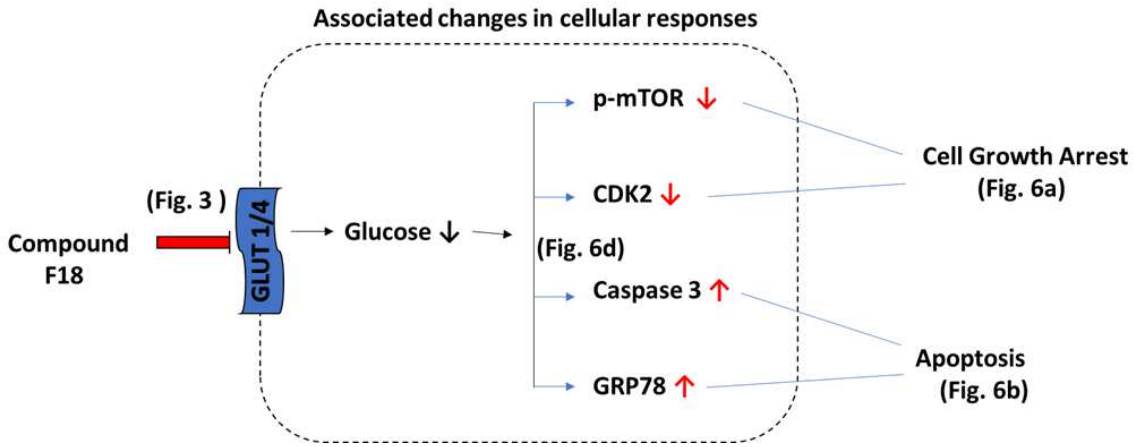

Figure 8. Schematic depiction of the proposed mode of action for compound F18 in CEM cells.

4. Materials and methods

4.1. Chemistry

4.1.1. General

Commercial reagents were from S D Fine Chem (Chennai, India), Research Lab (Mumbai, India), or Sigma Aldrich (St. Louis, USA), and were procured from suppliers in India. Thin layer chromatography was performed on Merck pre-coated Silica Gel 60 F254. Melting points (M.P.) were determined by the open capillary method on a VEEGO melting point apparatus and are uncorrected. Infrared spectra were recorded on Schimadzu FT/IR-8400S by direct sampling technique. ^{1}H and ^{13}C NMR spectra were recorded at 400 MHz on a Bruker instrument using tetramethylsilane (TMS) as internal standard, and chemical shifts (δ) are reported in ppm. J values for coupling constants are in hertz (Hz). Abbreviations used in NMR interpretation are: bs - broad singlet, s - singlet, d - doublet, t - triplet and m - multiplet. Mass spectra were recorded on a LC-MS Agilent Technologies 1260 Infinity instrument. The purity of final derivatives (≥95%) was confirmed by HPLC (high-performance liquid chromatography) on an Agilent 1100 system. The conditions for chromatography were: column - Hemochrome C18, 15 cm; detection wavelength - 300 nm; detector - UV visible detector; flow rate - 1 mL/min; oven temperature 30 °C; gradient elution with a run time of 15 min on mobile phase - Methanol: (0.1%) formic acid (FA) in a ratio 70:30. The chemical synthesis scheme is in **Fig. 2**.

4.1.2. Synthesis of intermediate, *[5-(Furan-2-ylmethylene)thiazolidine-2,4-dione] (5)*.

Furfuraldehyde **3** (5 ml, 0.07 mol), thiazolidine-2,4-dione **4** (5 g, 0.04 mol) and sodium acetate (3 g, 0.03 mol) were added to 5 ml of acetic acid and refluxed for 5 h. The reaction mixture was then cooled to room temperature (RT), and precipitated solid was collected by filtration under vacuum, then washed several times with water and dried at RT. Crude solid was purified by recrystallization from appropriate solvent to obtain brown shiny crystals of **5**.

Yield 7.7 g (68%); M.P. 238.4 °C; Brown shiny crystals; IR (cm^{-1}) 3234.73, 3140.22, 3010.98, 1674.27, 1604.83, 1543.10, 1512.24, 1263.42, 1147.68; ^{1}H NMR (400 MHz, DMSO-d6, δ ppm) 6.72-6.73 (m, 1H), 7.06 (d, J = 3.6 Hz, 1H), 7.5 (s, 1H), 12.43 (s, 1H).

4.1.3. Synthesis of intermediate, *Potassium-5-(furan-2-ylmethylene)-2,4-dioxothiazolidin-3-ide (6)*.

To the solution of potassium hydroxide (2.5 g, 0.044 mol) in 25 ml of ethanol, **4** (5 g, 0.025 mol) was added with stirring, and the reaction mixture was refluxed for 3 h. A fine light brown solid was obtained after cooling the reaction mixture, which was collected by filtering and washed with cold ethanol to obtain potassium salt **6.**

Yield 4.9 g (94 %); M.P. 269.9 °C (charred); Light brown solid; IR (cm^{-1}) 3037.99, 1662.69, 1626.05, 1585.54, 1531.53, 1139.97, 1226.77; ^{1}H NMR (400 MHz, DMSO-d_6, δ ppm) 6.56-6.59 (m, 2H), 7.06 (s, 1H), 7.75-7.76 (m, 1H).

4.1.4. Condensation of 6 with 2a-2y to produce F1-F25 (Figure 2).

Differently substituted chloroacetylated amides **(2a-2y)** were prepared according to our previous work[40,46,71]. Acetone (10 ml) was transferred in RBF, into which variously substituted chloroacetylated amides (**2a-2y)** and **6** (in equimolar ratio) were added and refluxed for 3-6 hrs and monitored by TLC for completion. After completion, the reaction was stopped and cooled. Acetone layer was evaporated to obtain a crude product, which was purified by either recrystallization from an appropriate solvent or by column chromatography (Ethyl acetate: Hexane, 1:4) to produce **F1-F25**.

2-(5-(Furan-2-ylmethylene)-2,4-dioxothiazolidin-3-yl)-N-phenylacetamide (F1)

Yield 42.5%; M.P. 234.7 °C (Charred); Buff white color solid; IR (cm^{-1}) 3269, 1741, 1689, 1614, 1599, 1111, 1255; ^{1}H NMR (400 MHz, DMSO-d_6, δ ppm) 4.41 (s, 2H), 6.78-6.79 (m, 1H), 7.06-7.10 (t, J = 7.2 Hz, 1H), 7.18-7.19 (d, J = 3.6 Hz, 1H), 7.30-7.34 (t, J = 7.8 Hz, 2H), 7.54-7.56 (d, J = 8 Hz, 2H), 7.82 (s, 1H), 8.10 (s, 1H), 10.39 (s, 1H); ^{13}CNMR (400 MHz, DMSO-d_6) 43.84, 113.68, 117.50, 149.113, 119.60, 119.96, 123.70, 128.85, 138.32, 147.97, 163.81, 165.07, 167.85; UV spectrum (10 ppm) λ_{max} 349 nm; MS (m/z) 327.0, 328.0 $[M-H]^{+}$; HPLC Purity % Area 99.61, retention time (RT) 4.58 mins.

N-(2-fluorophenyl)-2-(5-(furan-2-ylmethylene)-2,4-dioxothiazolidin-3-yl)acetamide (F2)

Yield 44.5%; M.P. 248.4 °C (Charred); Buff white color solid; IR (cm^{-1}) 3269, 1741, 1668, 1616, 1602, 1112, 1263, 1383; ^{1}H NMR (400 MHz, DMSO-d_6, δ ppm) 4.46 (s, 2H), 6.77-6.79 (m, 1H), 7.14-7.18 (m, 3H), 7.25-7.30 (m, 1H), 7.81-7.86 (m, 2H), 8.09 (s, 1H), 10.26 (s, 1H); ^{13}CNMR (400 MHz, DMSO-d_6) 43.68, 113.680, 115.471, 149.107, 115.661, 117.510, 119.590, 119.967, 123.679, 123.800, 124.474, 125.332, 125.628, 147.959, 164.443, 165.041, 167.832; UV spectrum (10 ppm) λ_{max} 350.3 nm;. MS (m/z) 345.0, 346.2 $[M-H]^{+}$; HPLC Purity % Area 99.71, RT 4.52 mins.

N-(3-fluorophenyl)-2-(5-(furan-2-ylmethylene)-2,4-dioxothiazolidin-3-yl) acetamide (F3)

Yield 50.2%; M.P. 250.2 °C (Charred); Brown color solid; IR (cm^{-1}) 3269, 1737, 1681, 1612, 1599, 1111, 1263, 1371; ^{1}H NMR (400 MHz, DMSO-d_6, δ ppm) 4.50 (s, 2H), 6.74-6.79 (m, 1H), 6.89-6.94 (m, 1H), 7.18-7.19 (d, 1H), 7.27-7.29 (m, 1H), 7.34-7.40 (m, 1H), 7.50-7.53 (d, 1H), 7.82 (s, 1H), 8.10 (s, 1H), 10.62 (s, 1H); ^{13}CNMR (400 MHz, DMSO-d_6) 43.86, 113.693, 114.910 149.100, 117.428, 119.652, 120.036, 130.523, 130.617, 139.933, 140.043, 147.995, 160.897, 163.298, 164.273, 165.031, 167.826; UV spectrum (10 ppm) λ_{max} 349.8nm; MS (m/z) 345.0, 346.0 $[M-H]^{+}$; HPLC Purity % Area 98.85, RT 5.61 mins.

N-(4-bromo-2,6-difluorophenyl)-2-(5-(furan-2-ylmethylene)-2,4-dioxothiazolidin-3-yl)acetamide (F4)

Yield 48.7%; M.P. 279.5 °C (Charred); Brownish solid; IR (cm^{-1}) 3269, 1745, 1680, 1695, 1618, 1545, 1114, 1379, 665; ^{1}H NMR (400 MHz, DMSO-d_6, δ ppm) 4.51 (s, 2H), 6.77 (s, 1H), 7.17 (d, J = 3.2 Hz, 1H), 7.43-7.48 (m, 1H), 7.58 (d, J = 8 Hz, 1H), 7.81 (s, 1H), 8.08 (s, 1H), 10.19 (s, 1H); ^{13}CNMR (400 MHz, DMSO-d_6) 43.172, 104.256, 104.515, 104.775, 113.671, 115.725, 116.011, 117.557, 119.554, 119.933, 123.217, 123.370, 147.948, 149.095, 164.579, 164.899, 167.689; UV spectrum (10 ppm) λ_{max} 349.5 nm; MS (m/z) 440.9, 442.9 $[M-H]^+$; HPLC Purity % Area 97.97, RT 4.61 mins.

N-(2,4-difluorophenyl)-2-(5-(furan-2-ylmethylene)-2,4-dioxothiazolidin-3-yl)acetamide (F5)

Yield 44.4%; M.P. 227.8 °C (Charred); Buff white color solid; IR (cm^{-1}) 3267, 1737, 1664, 1612, 1537, 1099, 1259, 1141; ^{1}H NMR (400 MHz, DMSO-d_6, δ ppm) 4.55 (s, 2H), 6.77-6.78 (m, 1H), 7.07 (t, J = 8.2 Hz, 1H), 7.17 (d, J = 3.6 Hz, 1H), 7.31-7.36 (m, 1H), 7.77-7.85 (m, 2H), 8.09 (s, 1H), 10.26 (s, 1H); ^{13}C NMR (400 MHz, DMSO-d_6) 43.578, 103.977, 104.216, 104.483, 111.098, 111.316, 113.681, 117.496, 119.599, 119.971, 121.844, 125.276, 147.968, 149.100, 164.509, 165.019, 167.816; UV spectrum (10 ppm) λ_{max} 351.3 nm; MS (m/z) 363.0, 364.0 $[M-H]^+$; HPLC Purity % Area 99.60, RT 4.97 mins.

2-(5-(Furan-2-ylmethylene)-2,4-dioxothiazolidin-3-yl)-N-(3-(trifluoromethyl)phenyl) acetamide (F6)

Yield 46.3%; M.P. 216.7 °C (Charred); Yellowish brown solid; IR (cm^{-1}) 3271, 1691, 1658, 1618, 1554, 1116, 1155; ^{1}H NMR (400 MHz, DMSO-d_6, δ ppm) 4.53 (s, 2H), 6.78 (t, J = 1.6 Hz, 1H), 7.18 (d, J = 3.2 Hz, 1H), 7.44 (d, J = 7.6 Hz, 1H), 7.58 (t, J = 8 Hz, 1H), 7.73 (d, J = 8 Hz, 1H), 7.82 (s, 1H), 8.04 (s, 1H), 8.10 (s, 1H), 10.26 (s, 1H); ^{13}CNMR (400 MHz, DMSO-d_6) 43.875, 113.692, 115.209, 117.413, 119.665, 120.052, 122.745, 125.316, 129.399, 129.713, 130.177, 139.040, 148.000, 149.094, 164.567, 165.031, 167.839; UV spectrum (10 ppm) λ_{max} 349.9 nm; MS (m/z) 395.0, 396.0 $[M-H]^+$; HPLC Purity % Area 97.79, RT 8.95 mins.

N-(4-chloro-2-(trifluoromethyl)phenyl)-2-(5-(furan-2-ylmethylene)-2,4-dioxothiazolidin-3-yl)acetamide (F7)

Yield 41.5%; M.P. 274.4 °C (Charred); Buff white color solid; IR (cm^{-1}) 3275, 1739, 1680, 1618, 1545, 1124, 1273, 1159, 746; ^{1}H NMR (400 MHz, DMSO-d_6, δ ppm) 4.51 (s, 2H), 6.77 (d, J = 1.6 Hz, 1H), 7.17 (d, J = 3.6 Hz, 1H), 7.51 (d, J = 8.4 Hz, 1H), 7.76-7.83 (m, 3H), 8.08 (s, 1H), 10.17 (s, 1H); ^{13}CNMR (400 MHz, DMSO-d_6) 43.416, 113.673, 117.503, 119.575, 119.948, 121.114, 123.837, 126.396, 131.352, 131.797, 133.114, 133.448, 147.955, 149.093, 164.934, 165.442, 167.703; UV spectrum (10 ppm) λ_{max} 350.9 nm; MS (m/z) 429.0, 430.9, 429.9 $[M-H]^+$; HPLC Purity % Area 98.72, RT 7.93 mins.

2-(5-(Furan-2-ylmethylene)-2,4-dioxothiazolidin-3-yl)-N-(4-methylbenzo[d]thiazol-2-yl)acetamide (F8)

Yield 47.5%; M.P. 220.2 °C (Charred); Pale yellow solid; IR (cm^{-1}) 3302, 2941, 1712, 1666, 1610, 1548, 1147, 1284; ^{1}H NMR (400 MHz, DMSO-d_6, δ ppm) 2.57 (s, 3H), 4.66 (s, 2H), 6.78 (d, J = 1.2 Hz, 1H), 7.18 (d, J = 3.6 Hz, 1H), 7.22 (d, J = 7.6 Hz, 1H), 7.26 (d, J = 6.8 Hz, 1H), 7.78 (d, J = 7.6 Hz, 1H), 7.82 (s, 1H), 8.09 (s, 1H), 12.92 (s, 1H); ^{13}CNMR (400 MHz, DMSO-d_6) 17.843, 43.345, 113.698, 117.402, 119.125, 119.707, 120.141, 123.785, 126.715, 130.065, 131.103, 147.503, 148.026, 149.089, 164.924, 167.823; UV spectrum (10 ppm) λ_{max} 350.2 nm; MS (m/z) 398.0, 399.0 $[M-H]^+$; HPLC Purity % Area 999.4, RT 14.09 mins.

2-(5-(Furan-2-ylmethylene)-2,4-dioxothiazolidin-3-yl)-N-(4-phenoxyphenyl)acetamide (F9)

Yield 45.6%; M.P. 163.5 °C (Charred); Brown color solid; IR (cm^{-1}) 3269, 1739, 1678, 1618, 1529, 1109, 1153, 1230, 1267; ^{1}H NMR (400 MHz, DMSO-d_6, δ ppm) 4.53 (s, 2H), 6.78 (s, 1H), 6.87 (d, J = 3.6Hz, 1H), 7.04 (d, J = 8 Hz, 2H), 7.11 (s, 2H), 7.17 (d, J = 4 Hz, 2H), 7.41(t, J = 7.4 Hz, 2H), 7.80 (s, 1H), 7.98 (s, 1H), 8.09 (s, 1H), 10.05 (s, 1H); ^{13}CNMR (400 MHz, DMSO-d_6) 43.772, 113.677, 117.516, 118.431, 118.713, 119.561, 119.927, 123.150, 123.535, 123.632, 125.207, 129.012, 129.947, 147.340, 147.946, 149.114, 156.449, 164.354, 165.048, 167.804; UV spectrum (10 ppm) λ_{max} 349.7 nm; MS (m/z) 418.8, 420.1 $[M-H]^+$; HPLC Purity: % Area 97.67, RT 10.62 mins.

N-(2-chloro-5-(trifluoromethyl)phenyl)-2-(5-(furan-2-ylmethylene)-2,4-dioxothiazolidin-3-yl)acetamide (F10)

Yield 44.5%; M.P. 242.6 °C (Charred); Buff white color solid; IR (cm^{-1}) 3261, 1739, 1678, 1614, 1587, 1126, 1265, 1265, 819; ^{1}H NMR (400 MHz, DMSO-d_6, δ ppm) 4.65 (s, 2H), 6.77 (s, 1H), 7.18 (d, J = 2.8 Hz, 1H), 7.56 (d, J = 8 Hz, 1H), 7.77 (d, J = 8.4 Hz, 1H), 7.82 (s, 1H), 8.09 (s, 1H), 8.16 (s, 1H), 10.33 (s, 1H); ^{13}CNMR (400 MHz, DMSO-d_6) 43.727, 113.676, 117.414, 119.640, 120.041, 121.373, 122.726, 124.841, 127.918, 128.240, 130.885, 135.135, 147.985, 149.089, 164.997, 165.250, 167.815; UV spectrum (10 ppm) λ_{max} 350.4 nm; MS (m/z) 431.0, 429.9 $[M-H]^+$; HPLC Purity % Area 96.76, RT 9.95 mins.

N-(4-bromo-2-fluorophenyl)-2-(5-(furan-2-ylmethylene)-2,4-dioxothiazolidin-3-yl)acetamide (F11)

Yield 48.2%; M.P. 257.6 °C (Charred); Buff white color solid; IR (cm^{-1}) 3261, 1739, 1668, 1614, 1593, 1112, 1273, 1381, 761; ^{1}H NMR (400 MHz, DMSO-d_6, δ ppm) 4.57(s, 2H), 6.77 (s, 1H), 7.17 (d, J = 3.2 Hz, 1H), 7.38 (d, J = 8.8 Hz, 1H), 7.61 (d, J = 10.4Hz, 1), 7.81-7.89 (m, 2H), 8.08 (s, 1H), 10.37 (s, 1H); ^{13}CNMR (400 MHz, DMSO-d_6) 43.701, 113.673, 115.975, 116.059, 117.448, 118.796, 119.022, 119.611, 120.005, 124.876, 125.056, 125.170, 127.534, 127.568, 147.962, 149.092, 164.601, 165.003, 167.811; UV spectrum (10 ppm) λ_{max} 349.3nm; MS (m/z) 424.9, 423.0 $[M-H]^+$; HPLC Purity % Area 98.50, RT 8.79 mins.

2-(5-(Furan-2-ylmethylene)-2,4-dioxothiazolidin-3-yl)-N-(4-methoxyphenyl) acetamide (F12)

Yield 52.5%; M.P. 246 °C (Charred); Pale yellow solid; IR (cm^{-1}) 3286, 1737, 1667, 1640, 1546, 1111, 1284, 1149; ^{1}H NMR (400 MHz, DMSO-d_6, δ ppm) 3.72 (s,3H), 4.46 (s, 2H), 3.78-3.79 (m, 1H), 6.90 (d, J = 9, 2H), 7.19 (d, J = 3.48, 1H), 7.46(d, J = 9.04, 2H), 7.82 (s, 1H), 8.10 (d, J = 1.56 Hz, 1H), 10.22 (s, 1H); ^{13}C NMR (400 MHz, DMSO-d_6) 43.331, 54.953, 111.396, 124.271, 125.202, 127.980, 129.492, 129.711, 137.617, 139.449, 149.322, 150.965, 159.528, 163.947, 165.532, 171.024; UV spectrum (10 ppm) λ_{max} 350.1 nm; MS (m/z) 357.0, 357.8 $[M-H]^{+}$; HPLC Purity % Area 99.53, RT 4.33 mins.

N-(4-fluorophenyl)-2-(5-(furan-2-ylmethylene)-2,4-dioxothiazolidin-3-yl) acetamide (F13)

Yield 42.5%; M.P. 240.8 °C (Charred); Brownish solid; IR (cm^{-1}) 3286, 1743, 1676, 1612, 1545, 1105, 1217, 1149; ^{1}H NMR (400 MHz, DMSO-d_6, δ ppm) 4.48 (s, 2H), 6.77-6.78 (m, 1H), 7.14-7.18 (m, 3H), 7.54-7.58 (m, 2H),7.80 (s, 1H), 8.08 (s, 1H), 10.46 (s, 1H); ^{13}CNMR (400 MHz, DMSO-d_6) 43.737, 113.695, 115.333, 115.554, 117.478, 119.612, 119.984, 120.976, 121.055, 134.647, 134.670, 147.946, 149.079, 157.007, 159.396, 163.803, 165.067, 167.881; UV spectrum (10 ppm) λ_{max} 345.2 nm; MS (m/z) 345.0, 345.9 $[M-H]^{+}$; HPLC Purity % Area 99.5, RT 5.09 mins.

2-(5-(Furan-2-ylmethylene)-2,4-dioxothiazolidin-3-yl)-N-(4-nitrophenyl) acetamide (F14)

Yield 47.5%; M.P. 277.5 °C (Charred); Pale yellow solid; IR (cm^{-1}) 3267, 1735, 1670, 1614, 1595, 1103, 1217, 1496; ^{1}H NMR (400 MHz, DMSO-d_6, δ ppm) 4.57 (s, 2H), 6.78 (d, J = 1.2 Hz, 1H), 7.18 (d, J = 3.2 Hz, 1H), 7.79-7.82 (m, 3H), 8.09 (s, 1H), 8.23 (d, J = 9.2 Hz, 2H), 11.02 (s, 1H); ^{13}CNMR (400 MHz, DMSO-d_6) 44.017, 113.710, 117.336, 119.004, 119.725, 120.129, 125.046, 142.587, 144.355, 148.026, 149.078, 164.968, 164.990, 167.818; UV spectrum (10 ppm) λ_{max} 348.8 nm; MS (m/z) 371.9, 373.0 $[M-H]^{+}$; HPLC Purity % Area 96.95, RT 6.94 mins.

2-(5-(Furan-2-ylmethylene)-2,4-dioxothiazolidin-3-yl)-N-(5-methylisoxazol-3-yl)acetamide (F15)

Yield 41%; M.P. 253.6 °C (Charred); Buff white color solid; IR (cm^{-1}) 3288, 2985, 1732, 1689, 1610, 1564, 1105, 1267, 1377; ^{1}H NMR (400 MHz, DMSO-d_6, δ ppm) 2.36 (s, 3H), 4.50 (s, 2H), 6.56 (s, 1H), 6.77 (s, 1H), 7.16 (d, J = 3.2 Hz, 1H), 7.8 (s, 1H), 8.07 (s, 1H), 11.02 (s, 1H); ^{13}CNMR (400 MHz, DMSO-d_6) 12.038, 43.531, 96.114, 113.688, 117.426, 119.642, 120.034, 147.958, 149.060, 157.534, 164.961, 167.828, 169.956; UV spectrum (10 ppm) λ_{max} 351.1 nm; MS (m/z) 332.0, 333.0 $[M-H]^{+}$; HPLC Purity % Area 99.48, RT 3.66 mins.

2-(5-(Furan-2-ylmethylene)-2,4-dioxothiazolidin-3-yl)-N-(thiazol-2-yl) acetamide (F16)

Yield 41.5%; M.P. 223.4 °C (Charred); Buff white color solid; IR (cm^{-1}) 3290, 1726, 1680, 1608, 1564, 1109, 1280; ^{1}H NMR (400 MHz, DMSO-d_6, δ ppm) 4.60 (s, 2H), 6.78-6.79 (m, 1H),

7.18 (d, J = 3.2 Hz, 1H), 7.25 (d, J = 3.6 Hz, 1H), 7.49 (d, J = 3.6 Hz, 1H), 7.82 (s, 1H), 8.10 (s, 1H), 12.58 (s, 1H); ^{13}CNMR (400 MHz, DMSO-d_6) 43.182, 113.710, 114.027, 117.413, 119.709, 120.099, 137.759, 148.028, 149.085, 164.956, 167.825; UV spectrum (10 ppm) λ_{max} 351.8 nm; MS (m/z) 333.9, 335.0 $[M-H]^+$; HPLC Purity % Area 96.04, RT 3.88 mins.

N-(3-chloro-4-methylphenyl)-2-(5-(furan-2-ylmethylene)-2,4-dioxothiazolidin-3-yl)acetamide (F17)

Yield 40.3%; M.P. 228.1 °C (Charred); Light brown solid; IR (cm^{-1}) 3263, 3041, 1743, 1687, 1618, 1585, 1112, 1274, 815; ^{1}H NMR (400 MHz, DMSO-d_6, δ ppm) 2.26 (s, 3H), 4.48 (s, 2H), 6.77 (t, J = 1.6 Hz, 1H), 7.17 (d, J = 3.2 Hz, 1H), 7.27-7.34 (m, 2H), 7.72 (d, J = 0.8 Hz, 1H), 7.81 (s, 1H), 8.08 (s, 1H), 10.50 (s, 1H); ^{13}CNMR (400 MHz, DMSO-d_6) 18.870, 43.812, 113.677, 117.455, 117.795, 119.166, 119.612, 119.995, 130.442, 131.296, 133.066, 137.377, 147.956, 149.093, 164.034, 165.039, 167.846; UV spectrum (10 ppm) λ_{max} 350.2 nm; MS (m/z) 375.0, 375.8 $[M-H]^+$; HPLC Purity % Area 96.53, RT 10.01 mins.

N-(benzo[d]thiazol-2-yl)-2-(5-(furan-2-ylmethylene)-2,4-dioxothiazolidin-3-yl)acetamide (F18)

Yield 38.5%; M.P. 220.2 °C (Charred); Buff white color solid; IR (cm^{-1}) 3223, 1735, 1662, 1602, 1545, 1112, 1257; ^{1}H NMR (400 MHz, DMSO-d_6, δ ppm) 4.67 (s, 2H), 6.79 (t, J = 1.6 Hz, 1H), 7.19 (d, J = 3.2 Hz, 1H), 7.33 (t, J = 7.4 Hz, 1H), 7.46 (t, J = 7.8 Hz, 1H), 7.77 (d, J = 8 Hz, 1H), 7.83 (s, 1H), 7.98 (d, J = 8 Hz, 1H), 8.10 (s,1H), 12.87 (s, 1H); ^{13}CNMR (400 MHz, DMSO-d_6) 43.423, 113.723, 117.381, 119.754, 120.180, 121.787, 123.853, 126.275, 148.050, 149.083, 164.945, 167.840; UV spectrum (10 ppm) λ_{max} 349.4 nm; MS (m/z) 384.0, 384.8 $[M-H]^+$; HPLC Purity % Area 97.36, RT 8.82 mins.

N-(3,4-dichlorophenyl)-2-(5-(furan-2-ylmethylene)-2,4-dioxothiazolidin-3-yl) acetamide (F19)

Yield 46%; M.P. 246.2 °C (Charred); Buff white color solid; IR (cm^{-1}) 3302, 1735, 1668, 1608, 1587, 1288, 817; ^{1}H NMR (400 MHz, DMSO-d_6, δ ppm) 4.51 (s, 2H), 6.77-6.78 (m, 1H), 7.17 (d, J = 3.2 Hz,1H), 7.45 (dd, J = 8.8 Hz, 1H), 7.57 (d, J = 8 Hz, 1H), 7.81 (s, 1H), 7.91 (d, J = 2.4 Hz, 1H), 8.08 (s, 1H), 10.71 (s, 1H); ^{13}CNMR (400 MHz, DMSO-d_6): 43.863, 113.684, 117.391, 119.252, 119.655, 120.061, 120.450, 125.272, 130.800, 131.118, 138.324, 147.980, 149.083, 164.471, 164.998, 167.818; UV spectrum (10 ppm) λ_{max} 350.1 nm; MS (m/z) 395.0, 396.9 $[M-H]^+$; HPLC Purity % Area 99.13, RT 13.18 mins.

N-(1,5-dimethyl-3-oxo-2-phenyl-2,3-dihydro-1H-pyrazol-4-yl)-2-(5-(furan-2-ylmethylene)-2,4-dioxothiazo lidin-3-yl)acetamide (F20)

Yield 42.5%; M.P. 254.7 °C (Charred); Brownish solid; IR (cm^{-1}) 3201, 1735, 1708, 1680, 1616, 1593, 1109, 1288; ^{1}H NMR (400 MHz, DMSO-d_6, δ ppm) 2.10 (s, 3H), 3.04 (s, 3H), 4.45 (s, 2H), 6.77 (s, 1H), 7.16 (d, J = 3.2 Hz, 1H), 7.34 (d, J = 8.4 Hz, 3H)7.50 (t, J = 7.6 Hz, 2H),

7.81 (s, 1H), 8.08 (s, 1H) 10.71(s, 1H); ^{13}CNMR (400 MHz, DMSO-d_6) 11.117, 35.825, 43.347, 106.474, 113.658, 117.653, 119.492, 119.834, 123.682, 126.399, 129.086, 134.839, 147.910, 149.122, 152.062, 161.423, 164.732, 165.046, 167.819; UV spectrum (10 ppm) λ_{max} 349.3 nm; MS (m/z) 439.1 $[M-H]^+$; HPLC Purity % Area 98.25, RT 3.41 mins.

N-(4-bromophenyl)-2-(5-(furan-2-ylmethylene)-2,4-dioxothiazolidin-3-yl)acetamide (F21)

Yield 45.5%; M.P. 242.2 °C (Charred); Buff white color solid; IR (cm^{-1}) 3254, 1743, 1687, 1614, 1591, 1111, 1274, 815; ^{1}H NMR (400 MHz, DMSO-d_6, δ ppm) 4.49 (s, 2H), 6.78 (s, 1H), 7.18 (s, 1H), 7.51 (s, 4H), 7.81 (s, 1H), 8.09 (s, 1H), 10.53 (s, 1H); ^{13}CNMR (400 MHz, DMSO-d_6) 43.868, 113.681, 115.338, 117.463, 119.620, 120.007, 121.131, 131.676, 137.672, 147.974, 149.102, 164.056, 165.035, 167.824; UV spectrum (10 ppm) λ_{max} 350.3 nm; MS (m/z) 406.9, 405.1 $[M-H]^+$; HPLC Purity % Area 96.4, RT 8.53 mins.

2-(5-(Furan-2-ylmethylene)-2,4-dioxothiazolidin-3-yl)-N-(pyridin-2-yl) acetamide (F22)

Yield 35.5%; M.P. 230.1 °C (Charred); Pale yellow solid; IR (cm^{-1}) 3117, 1730, 1674, 1614, 1583, 1105, 1205; ^{1}H NMR (400 MHz, DMSO-d_6, δ ppm) 4.56 (s, 2H), 6.77-6.79 (m, 1H), 7.12 (dd, J = 6.8 Hz, 1H), 7.18 (d, J = 3.6 Hz, 1H), 7.77 (d, J = 1.2 Hz, 1H), 7.81 (s, 1H), 7.96 (m, 1H), 8.09 (d, J = 0.8 Hz, 1H), 8.34 (d, J = 4 Hz, 1H), 10.53 (s, 1H); ^{13}CNMR (400 MHz, DMSO-d_6) 43.827, 113.489, 113.688, 117.494, 119.613, 119.846, 119.986, 138.397, 147.978, 148.085, 149.107, 151.309, 165.047, 167.848; UV spectrum (10 ppm) λ_{max} 350.3 nm; MS (m/z) 330.0, 331.0 $[M-H]^+$; HPLC Purity % Area 97.43, RT 3.79 mins.

2-(5-(Furan-2-ylmethylene)-2,4-dioxothiazolidin-3-yl)-N-(p-tolyl)acetamide (F23)

Yield 49.5%; M.P. 268.2 °C (Charred); Buff white color solid; IR (cm^{-1}) 3267, 3041, 1687, 1658, 1618, 1597, 1111, 1257; ^{1}H NMR (400 MHz, DMSO-d_6, δ ppm) 2.25 (s, 3H), 4.47 (s, 2H), 6.78 (t, J = 1.6 Hz, 1H), 7.12 (d, J = 8.4 Hz, 2H), 7.18 (d, J = 3.2 Hz, 1H), 7.43 (d, J = 8.4 Hz, 2H), 7.81 (s, 1H), 8.09 (s, 1H), 10.29 (s, 1H); ^{13}CNMR (400 MHz, DMSO-d_6) 43.803, 113.675, 117.543, 119.165, 119.565, 119.927, 129.214, 132.680, 135.822, 147.948, 149.116, 163.547, 165.083, 167.854; UV spectrum (10 ppm) λ_{max} 350.5 nm; MS (m/z) 340.9, 341.2, 342.0 $[M-H]^+$; HPLC Purity % Area 96.44, RT 5.75 mins.

N-(3,4-dibromophenyl)-2-(5-(furan-2-ylmethylene)-2,4-dioxothiazolidin-3-yl)acetamide (F24)

Yield 41.2%; M.P. 247.2 °C (Charred); Buff white color solid; IR (cm^{-1}) 3255, 1735, 1672, 1610, 1585, 1111, 1288, 536; ^{1}H NMR (400 MHz, DMSO-d_6, δ ppm) 4.50 (s, 2H), 6.78 (s, 1H), 7.18 (d, J = 2.8 Hz, 1H), 7.46 (d, J = 8.8 Hz, 1H), 7.58 (d, J = 8.8 Hz, 1H), 7.81 (s, 1H), 7.91 (s, 1H), 8.09 (s, 1H), 10.71 (s, 1H); ^{13}CNMR (400 MHz, DMSO-d_6) 43.862, 113.699, 117.389, 119.269, 119.673, 120.068, 120.457, 125.273, 130.817, 131.114, 138.321, 147.992, 149.078,

164.481, 165.003, 167.824; UV spectrum (10ppm) λ_{max} 350nm; MS (m/z) 394.9, 396.9 $[M-H]^+$; HPLC Purity % Area 99.27, RT 13.08 mins.

2-(5-(Furan-2-ylmethylene)-2,4-dioxothiazolidin-3-yl)-N-(4-methylthiazol-2-yl)acetamide (F25)

Yield 36%; M.P. 268.7 °C (Charred); Buff white color solid; IR (cm^{-1}) 3117, 2972, 1734, 1672, 1612, 1579, 1109, 1286, 1369; ^{1}H NMR (400 MHz, DMSO-d_6, δ ppm) 2.33 (s, 3H), 4.57 (s, 2H), 6.77-6.78 (m, 1H), 7.15 (d, 1H), 7.18 (d, 1H), 7.81 (s, 1H), 8.09 (s, 1H), 12.37 (s, 1H); ^{13}CNMR (400 MHz, DMSO-d_6) 11.045, 43.147, 113.708, 117.435, 119.681, 120.078, 126.854, 148.005, 149.079, 164.956, 167.824; UV spectrum (10 ppm) λ_{max} 350.8 nm; MS (m/z) 348.1, 349.0 $[M-H]^+$; HPLC Purity % Area 95.74, RT 13.1 mins.

4.2. GLUT1, GLUT4, and GLUT5 transport assay.

Synthesized compounds were examined for their effect on transport activity of human GLUT1[47], GLUT4[47], and GLUT5[72] expressed in hexose transporter null yeast cells (*hxt*^{0}). Yeast cell culturing was done at 30 ºC with shaking (180 rpm). VW4000*fgy1* yeast cells expressing GLUT1[47] were cultured for 2-3 days in the Synthetic Complete media without uracil (SC-uracil) with 2% (w/v) maltose. Cells were washed once in SC-uracil with 2% (w/v) glucose media, transferred in the same media at OD_{600nm}~0.5, and grown further for 1-2 days. VW4000*fgy1erg4* yeast cells expressing GLUT4[47] were cultured like GLUT1, but in media with lower concentrations of maltose and glucose: SC-uracil with 1% (w/v) maltose media for the initial cell culture, and SC-uracil with 0.2% (w/v) glucose media for the final cell culture. VW4000 yeast cells expressing GLUT5[72] were cultured for one day in YEP [1% (w/v) yeast and 2% (w/v) peptone] media with 2% (w/v) maltose and 100 µg/ml geneticin G418. Cells were washed once in YEP media with 2% (w/v) fructose and 100 µg/ml geneticin G418, transferred in the same media at OD_{600nm}~0.5, and grown further for 1-2 days. For transport assay, cells in the hexose media were centrifuged (1000xg, 5 minutes), washed once in PBS buffer (10 mM Na_2HPO_4, 1.8 mM KH_2PO_4, 2.7 mM KCl, 137 mM NaCl, pH 7.4), then resuspended in PBS buffer at an OD_{600nm} ~ 10; each assay contained 100 µl of this cell solution. Transport assay was started by the addition of C^{14}-hexose to a final concentration of 5 mM glucose for GLUT1 or GLUT4 and 10 mM fructose for GLUT5. Transport assay was stopped after 10 minutes by adding 3-ml ice-chilled Quench buffer (0.1 M KPi, 0.1 M LiCl, pH 5.5), followed by filtration on a glass fiber filter (GC50; Advantec, Tokyo, Japan) under vacuum, and another wash with 3-ml Quench buffer and filtration. The filtration membranes were transferred to scintillation vials, and 10 ml of Scintillation buffer (BioSafeII; Research Products International, Mount Prospect, IL, USA) was added in each vial. After brief vortexing, radioactivity was measured with a scintillation counter (Tri-carb 2900TR, Perkin Elmer, USA). As all synthesized compounds were solubilized in dimethyl sulfoxide (DMSO), controls for the determination of the relative activity included 1% (v/v) DMSO - to account for DMSO concentration in the transport assay due to

inhibitor addition - as well as saturating concentrations of known inhibitors for GLUTs [200 µM phloretin for GLUT1 and GLUT4[73], and 100 µM N-[4-(methylsulfonyl)-2-nitrophenyl]-1,3-benzodioxol-5-amine (MSNBA) for GLUT5[74]]. All inhibitors were added to the assay from stock concentrations so that the final concentration in the assay was 1% (v/v). Initial inhibition screening for TZD compounds was done at 100 µM concentration; for the compounds that decreased the relative transport activity by 50% or more, inhibitor concentration was varied in the transport assay from 0.1 to 100 µM to determine inhibitor IC_{50}. Data were analyzed with GraphPad Prism (San Diego, CA, USA).

4.3. Docking studies.

The SiteFinder function of Molecular Operation Environment (MOE, Chemical Computing Group, Montreal, Canada) was used to model the binding sites of compounds F18 and F19 in the 3D crystal structure of GLUT1 inward-facing conformation (PDB ID: 4PYP, www.rcsb.org), and a GLUT1 outward-facing homology model based on the GLUT3 crystal structure (PDB ID: 4ZWC, www.rcsb.org). The latter model was generated in MOE with the Homology Model function. Possible conformations of the compounds were generated with MOE Conformational Generation function; **F18** had 29 conformations, **F19** had 104 conformations. Virtual docking was carried out with the MOE Dock function with the Triangle Matcher placement scoring London dG and Rigid Receptor refinement scoring GBVI/WSA dG against the dummy atoms around the substrate binding site. Potential docking positions were selected with a selection criterion of the lowest energy scoring algorithm and verifying that the docking pocket has sufficient space for the compound binding and reasonable interactions with the protein residues. The homology models and docking were validated with Ramachandran plots and docking of the octyl glucoside, the original ligand in the crystal structure, to the GLUT1 crystal structure (**Supplementary Data, Figure S1)**.

4.4. Cell cultures.

Three human leukemia/lymphoma cancer cell lines (KCl-22, K562, and CCRF-CEM), one breast cancer cell line (MDA-MB-231), and one normal, non-cancerous, fibroblast cell line (HS-27) were used to test the cytotoxic potential of the synthetic derivatives. MDA-MB-231 and HS-27 cells were grown in DMEM medium (HyClone, Logan UT, USA) supplemented with 10% (v/v) FBS, 100 U/ml penicillin and 100 µg/ml streptomycin. The culture medium for the leukemic/lymphoid cancer cells was RPMI, supplemented in the same manner. Cell cultures were maintained at 37 °C in a humidified 5% CO_2 atmosphere. Cells were counted and seeded for experimental use upon reaching ≥90% viability and 65–75% confluence.

4.5. Cell viability assay by differential nuclear staining assay.

The Differential Nuclear Staining (DNS) assay is a live cell imaging-based assay, which utilizes two nuclear dyes to easily label living and dead cells[59]. An initial assessment of cytotoxicity on this series of 25 compounds was conducted via the DNS assay upon exposure of CCRF-CEM, K-562, KCL-22, and MDA-MB-231 human cancer cell lines to 50 μM of a compound for 48 hours. Compounds were dissolved and diluted in dimethyl sulfoxide (DMSO) to reach the desired concentration. DMSO, hydrogen peroxide, and untreated cells were the vehicle, positive and negative controls, respectively, in all experiments. Cells were seeded in 96-well plates at a density of 10,000 cells/well in 100 μL of complete culture media, with the exception of HS-27, for which only 3,000 cells/well were used to compensate for their large size. Cells were seeded in 96-well plates at a density of 10,000 cells/well in 100 μL of complete culture media. Images of stained cells were taken with the GE Healthcare Life Sciences IN Cell Analyzer 2200. Two hours before imaging, Hoechst, and propidium iodide (PI) stains were added to each well to distinguish living and dead/dying cells. Hoechst is a dye capable of permeating the membranes of all cells within a sample, whereas PI will only penetrate cells with compromised membranes. Colocalization of Hoechst (blue) and PI (red) signals indicate the dead cell population [59]. In this initial screening, experimental samples were assessed singularly, and control samples in quadruplicate. Subsequent DNS assays, using CCRF-CEM, K-562, KCl-22, and MDA-MB-231 cell lines, were then performed to determine the 50% cytotoxic concentration (CC_{50}) values of the seven compounds with the highest cytotoxicity in the initial screening. Similarly, the selective toxicity of the two most active compounds, F18 and F19, was assessed using the non-cancerous cell line HS-27. Cells were seeded identically but were treated with test compounds at concentrations ranging from 0.5 to 100 μM. Experimental samples and controls were evaluated for cytotoxicity in quadruplicate after 48 hours of incubation. Selectivity Index (SCI) values were calculated by dividing the CC_{50} for non-cancerous cell line HS-27 by the CC_{50} of each cancer cell line after 48 hours of incubation (SCI = Normal cell CC_{50} / Cancer cell CC_{50}). High SCI scores are suggestive of selective toxicity toward cancer cells, an effect which may or may not be conferred in vivo.

4.6. Apoptosis studies by flow cytometry.

The induction of apoptosis by compound **F18** was studied by flow cytometry, as described earlier[75]. Cells were seeded in a 24-well flat-bottom microplate and incubated overnight at 37 ^{0}C in a CO_2 incubator for 24 hrs. The cell media was replaced with fresh media, and then the cells were treated with IC_{50} concentration of F18 for 24 hrs. Untreated cells were used as negative control. Post incubation, cells were washed with PBS, then centrifuged for 5 minutes at 500 g at 4 °C, and the supernatant was discarded. Cell pellets were resuspended in ice-cold 1X Binding Buffer and then mixed with 1 μL of annexin V-FITC solution and 5 μL PI (propidium iodide). Tubes were kept on ice and incubated for 15 minutes in the dark, then 400 μL of ice-cold 1X Binding Buffer was added, and cell preparations were analyzed by flow cytometry (BD Accuri C5 flow cytometer, BD Biosciences, CA, USA). Cytometry data were analyzed with

FlowJo software (version 10.1, Ashland, OR, USA). All experimental treatments and controls were assessed in triplicate**.**

4.7. Cell cycle analysis by flow cytometry.

An asynchronous culture of CEM cells was seeded in 24-well plates at a density of 100,000 cells/well in 1 mL of complete culture media and treated with concentrations of compound F18 for 72 hours. Controls included in this experiment were DMSO, hydrogen peroxide, and untreated cells, as described above. Cells were treated with 50 μM, 25 μM, or 10 μM of compound **F18**. Concentrations of experimental treatments were chosen based on the CC_{50} value of the given compound. After 72 hours, cells were collected, centrifuged at 262 g for 5 minutes, and resuspended in 100 μL of complete culture media. Then, 200 μL of a nuclear isolation medium (NIM)-DAPI solution, which simultaneously permeabilizes the plasma membrane and stains DNA with the violet-excited DNA-intercalating agent DAPI, was added to each sample and immediately analyzed by flow cytometry. Approximately 100,000 events (cells) were analyzed per sample to obtain a well-defined cell cycle profile using the Kaluza flow cytometry software (Beckman Coulter)[76]. All experimental treatments and controls were assessed in triplicate**.**

4.8. Western blotting.

Western blotting was carried out as per the manufacture's protocol. Briefly, cells grown in multiwell dishes were washed twice with cold PBS, lysed in Laemmli buffer (62.5 mM Tris-HCl, pH 6.8, 10% (v/v) glycerol, 2% (w/v) SDS) supplemented with Complete protease inhibitors (Roche), and sonicated before protein quantification (DC BioRad Protein Assay Cat No. 500-0114). Samples with equal protein quantity were supplemented with 5% (v/v) β-mercaptoethanol, heated at 95 °C for 12 minutes, size-fractionated on a 9% SDS-PAGE gel, and transferred onto nitrocellulose membranes. All Blue Precision Plus Protein Standard (Bio-Rad Cat. No. 161-0373) was used as the protein size marker. Membranes were blocked for 45 minutes in PBS-T-milk (PBS buffer with 0.05% (v/v) Tween, 5% (w/v) dried fat-free milk), incubated with primary antibody diluted in PBS-T-milk (3 hours at room temperature), washed (PBS-T), and incubated with secondary antibody diluted in PBS-T-milk (1 hour at room temperature). After the removal of unbound secondary antibodies, signals were revealed using Super Signal West Femto Maximum Sensitivity Substrate (Pierce).

4.9. Isolation of WBCs and assessment of F18 effect on viability of non-transformed WBCs. Ethical clearance was obtained from the institutional ethical committee of Maratha Mandal's NGH Institute of Dental Sciences, Belagavi, for the collection of whole blood from healthy adult volunteer for the current study. This study was carried out in accordance with relevant guidelines and regulations and informed consent was obtained from the participant before collection of blood samples. A volume of 2.5 ml HiSep was transferred aseptically to a 15 ml clean centrifuge

tube and overlaid with 7.5 ml diluted blood without mixing and centrifuged at 400xg at room temperature for 30 minutes. The supernatant containing plasma and platelets was discarded. Ten milliliters of isotonic phosphate buffer were added, and the mononuclear cell suspension was centrifuged at 200xg at room temperature for 10 mins. Cells were washed with isotonic buffer and resuspended in an RBC lysis for 5 mins. Then the cells were centrifuged for 5 mins, the supernatant was discarded, and cells were washed with PBS twice and maintained in a CO_2 incubator at 37 ºC (95% humidity and 5% CO_2) till completion of MTT assay experiments. For the cytotoxicity test, isolated WBCs were seeded in a 96-well flat-bottom microplate and maintained at 37 ºC in 95% humidity and 5% CO_2 overnight. Cells were treated with different concentrations of **F18** and incubated for another 48 hours. The wells were washed twice with PBS, 20 µL of the MTT staining solution was added to each well, and the plate was incubated at 37 ºC. After 4 h, 100 µL of DMSO was added to each well to dissolve the formazan crystals, and absorbance was recorded at 570 nm using a microplate reader.

4.10. *In-vivo* tumor xenograft study in CEM mice model

4.10.1. Experimental dose determination.

SCID mice were housed in individually ventilated cage system in 12 h light dark cycle. The area was controlled for noise and humidity. Animals were fed autoclaved commercial pellets and water ad libitum. Animals were handled in a laminar air flow hood. Mice 8-10 weeks were used for the experiment. Five animals were administered 500 mg/kg and 1000 mg/kg single dose of **F18** i.p. Animals receiving 1000 mg/kg showed symptoms of distress, and two animals died. None of the animals receiving 500 mg/kg died. Clinical distress symptoms recovered within 6 hours. A tenth of this dose was selected for experimental work.

4.10.2. Tumor regression in CEM mice model (efficacy study).

SCID mice, 8-10 weeks old, housed, fed, and handled as described above, were used for the experiment. CEM cells $1x10^5$ were injected on the back of the mice and allowed to form palpable tumors. Tumors were minced and regrafted in experimental animals. The administration of the test sample was done after the tumor reached a palpable size. Doxorubicin 20 mg/kg i.p., F18 50 mg/kg i.p., were administered on day 1-5, 8-12, 15-18. Tumor volume was measured with a digital vernier calipers (Mitutoyo Japan). Tumor volume was calculated as: Volume = $(\text{width})^2$ x length/2. At the end of the experiment, the animals were sacrificed by cervical dislocation. The animals were dissected, and the excised tumors were imaged immediately.

4.11. HDAC enzyme activity assay.

Recombinant HDAC8 was produced as described recently[77]. Recombinant cHDAC4 was expressed in a pET14b vector (Novagen, EMD Millipore) containing the codon-optimized catalytic domain of human HDAC4. A serial dilution of inhibitor in assay buffer (25 mM Tris-HCl, pH 8.0, 75 mM KCl, 0.001% Pluronic F-127) was incubated with HDAC in a black 96-well

microtiter half-area plate (Greiner) for 60 min at 30 °C. Then, the reaction was initiated by the addition of 20 µM Boc-Lys(trifluoroacetyl)-AMC (Bachem) as the substrate for HDAC8 and HDAC4. After incubation for 60 min at 30 °C, the reaction was stopped by the addition of 1.7 µM SATFMK for HDAC4 and 8. The deacetylated substrate was converted into a fluorescent product by the addition of 0.4 mg/ml trypsin (Applichem). The release of AMC was followed in a microplate reader (PheraStar Plus, BMG Labtech) at 450 nm (λ_{Ex} = 350 nm) and correlated to enzyme activity. Dose-response curves were generated with GraphPad Prism and fitted to a four parameters logistic function to obtain IC_{50} values[78]:

$$EA = E_0 + \frac{(E_{max} - E_0)}{1 + 10^{(\log(IC_{50}) - x) * h}}$$

in which *EA* is enzyme activity at a given inhibitor concentration *x*, E_0 is enzyme activity determined at zero, and E_{max} is enzyme activity at complete inhibition. IC_{50} indicates the concentration of inhibitor at which half the enzyme is inhibited, and h is the curve slope.

Abbreviations.

TZD- Thiazolidinedione**,** GLUT1/4/5- Glucose transporter 1/4/5**,** HDAC-Histone deacetylase**,** DMF- Dimethyl Formamide**,** DMSO- dimethylsulfoxide**,** DCM- Dichloromethane**,** NMR- Nuclear magnetic resonance spectroscopy**,** IR- Infrared Spectroscopy, DMEM- Dulbecco's Modified Eagle Medium**,** MTT- 3-(4,5-dimethylthiazol-2-yl)-2,5-diphenyltetrazolium bromide**,** FBS- fetal calf serum**,** RPMI- Roswell Park Memorial Institute media**,** PBS- Phosphate-buffered saline, SCID-severe combined immunodeficiency, WBC-White blood cells.

References

[1] P.-B. Ancey, C. Contat, E. Meylan, Glucose transporters in cancer - from tumor cells to the tumor microenvironment, FEBS J. 285 (2018) 2926–2943. https://doi.org/10.1111/febs.14577.

[2] R.A. Cairns, I.S. Harris, T.W. Mak, Regulation of cancer cell metabolism, Nat. Rev. Cancer. 11 (2011) 85–95. https://doi.org/10.1038/nrc2981.

[3] A. Schulze, A.L. Harris, How cancer metabolism is tuned for proliferation and vulnerable to disruption, Nature. 491 (2012) 364–373. https://doi.org/10.1038/nature11706.

[4] M.G.V. Heiden, L.C. Cantley, C.B. Thompson, Understanding the Warburg Effect: The Metabolic Requirements of Cell Proliferation, Science. 324 (2009) 1029–1033. https://doi.org/10.1126/science.1160809.

[5] K. Adekola, S.T. Rosen, M. Shanmugam, Glucose transporters in cancer metabolism, Curr. Opin. Oncol. 24 (2012) 650–654. https://doi.org/10.1097/CCO.0b013e328356da72.

[6] S.K. McBrayer, J.C. Cheng, S. Singhal, N.L. Krett, S.T. Rosen, M. Shanmugam, Multiple myeloma exhibits novel dependence on GLUT4, GLUT8, and GLUT11: implications for glucose transporter-directed therapy, Blood. 119 (2012) 4686–4697. https://doi.org/10.1182/blood-2011-09-377846.

[7] C.C. Barron, P.J. Bilan, T. Tsakiridis, E. Tsiani, Facilitative glucose transporters: Implications for cancer detection, prognosis and treatment, Metabolism. 65 (2016) 124–139. https://doi.org/10.1016/j.metabol.2015.10.007.
[8] D. Deng, N. Yan, GLUT, SGLT, and SWEET: Structural and mechanistic investigations of the glucose transporters, Protein Sci. 25 (2016) 546–558. https://doi.org/10.1002/pro.2858.
[9] M. Mueckler, B. Thorens, The SLC2 (GLUT) family of membrane transporters, Mol. Aspects Med. 34 (2013) 121–138. https://doi.org/10.1016/j.mam.2012.07.001.
[10] X. Jin, Y. Liang, D. Liu, Q. Luo, L. Cai, J. Wu, L. Jia, W.-L. Chen, An essential role for GLUT5-mediated fructose utilization in exacerbating the malignancy of clear cell renal cell carcinoma, Cell Biol. Toxicol. 35 (2019) 471–483. https://doi.org/10.1007/s10565-019-09478-4.
[11] C. Wei, R. Bajpai, H. Sharma, M. Heitmeier, A.D. Jain, S.M. Matulis, A.K. Nooka, R.K. Mishra, P.W. Hruz, G.E. Schiltz, M. Shanmugam, Development of GLUT4-selective antagonists for multiple myeloma therapy, Eur. J. Med. Chem. 139 (2017) 573–586. https://doi.org/10.1016/j.ejmech.2017.08.029.
[12] S. Pragallapati, R. Manyam, Glucose transporter 1 in health and disease, J. Oral Maxillofac. Pathol. JOMFP. 23 (2019) 443–449. https://doi.org/10.4103/jomfp.JOMFP_22_18.
[13] Y. Noguchi, A. Saito, Y. Miyagi, S. Yamanaka, D. Marat, C. Doi, T. Yoshikawa, A. Tsuburaya, T. Ito, S. Satoh, Suppression of facilitative glucose transporter 1 mRNA can suppress tumor growth, Cancer Lett. 154 (2000) 175–182. https://doi.org/10.1016/s0304-3835(00)00392-x.
[14] E.M. Selwan, B.T. Finicle, S.M. Kim, A.L. Edinger, Attacking the supply wagons to starve cancer cells to death, FEBS Lett. 590 (2016) 885–907. https://doi.org/10.1002/1873-3468.12121.
[15] M.E. Figueroa, O. Abdel-Wahab, C. Lu, P.S. Ward, J. Patel, A. Shih, Y. Li, N. Bhagwat, A. Vasanthakumar, H.F. Fernandez, M.S. Tallman, Z. Sun, K. Wolniak, J.K. Peeters, W. Liu, S.E. Choe, V.R. Fantin, E. Paietta, B. Löwenberg, J.D. Licht, L.A. Godley, R. Delwel, P.J.M. Valk, C.B. Thompson, R.L. Levine, A. Melnick, Leukemic IDH1 and IDH2 Mutations Result in a Hypermethylation Phenotype, Disrupt TET2 Function, and Impair Hematopoietic Differentiation, Cancer Cell. 18 (2010) 553–567. https://doi.org/10.1016/j.ccr.2010.11.015.
[16] A.K. Coskun, R.E. Sutton, Expression of Glucose Transporter 1 Confers Susceptibility to Human T-Cell Leukemia Virus Envelope-Mediated Fusion, J. Virol. 79 (2005) 4150–4158. https://doi.org/10.1128/JVI.79.7.4150-4158.2005.
[17] R.C. Laister, M.D. Minden, T.W. Mak, Inhibition of Glycolysis as a Therapeutic Strategy in Acute Myeloid Leukemias, in: M. Andreeff (Ed.), Target. Ther. Acute Myeloid Leuk., Springer New York, New York, NY, 2015: pp. 709–723. https://doi.org/10.1007/978-1-4939-1393-0_38.
[18] H.A.R. Pontes, F.S.C. Pontes, B.S. de F. Silva, F.P. Fonseca, B.A.B. de Andrade, V.H.T. Rizo, M.J. Romanach, J.E. Leon, O.P. de Almeida, Extranodal Nasal NK/T-Cell Lymphoma: A Rare Oral Presentation and FASN, CD44 and GLUT-1 Expression, Braz. Dent. J. 24 (2013) 284–288. https://doi.org/10.1590/0103-6440201302202.
[19] T.E. Wood, S. Dalili, C.D. Simpson, R. Hurren, X. Mao, F.S. Saiz, M. Gronda, Y. Eberhard, M.D. Minden, P.J. Bilan, A. Klip, R.A. Batey, A.D. Schimmer, A novel inhibitor of glucose uptake sensitizes cells to FAS-induced cell death, Mol. Cancer Ther. 7 (2008) 3546–3555. https://doi.org/10.1158/1535-7163.MCT-08-0569.
[20] J. Bentley, I. Walker, E. McIntosh, A.D. Whetton, P.J. Owen-Lynch, S.A. Baldwin, Glucose transport regulation by p210 Bcr–Abl in a chronic myeloid leukaemia model, Br. J. Haematol. 112 (2001) 212–215. https://doi.org/10.1046/j.1365-2141.2001.02428.x.
[21] S. Sadiq, E. Owen, T. Foster, K. Knight, L. Wang, M. Pirmohamed, R.E. Clark, S. Pushpakom, Nilotinib-induced metabolic dysfunction: insights from a translational study using in vitro

adipocyte models and patient cohorts, Leukemia. 33 (2019) 1810–1814. https://doi.org/10.1038/s41375-018-0337-0.
[22] H.L. Wieman, S.R. Horn, S.R. Jacobs, B.J. Altman, S. Kornbluth, J.C. Rathmell, An essential role for the Glut1 PDZ-binding motif in growth factor regulation of Glut1 degradation and trafficking, Biochem. J. 418 (2009) 345–367. https://doi.org/10.1042/BJ20081422.
[23] J.Y. Chan, S. Kong, Y. Choy, C. Lee, K. Fung, Inhibition of glucose transporter gene expression by antisense nucleic acids in HL-60 leukemia cells, Life Sci. 65 (1999) 63–70. https://doi.org/10.1016/S0024-3205(99)00219-2.
[24] C. Granchi, S. Fortunato, F. Minutolo, Anticancer agents interacting with membrane glucose transporters, MedChemComm. 7 (2016) 1716–1729. https://doi.org/10.1039/C6MD00287K.
[25] H. Liao, Z. Wang, Z. Deng, H. Ren, X. Li, Curcumin inhibits lung cancer invasion and metastasis by attenuating GLUT1/MT1-MMP/MMP2 pathway, Int. J. Clin. Exp. Med. 8 (2015) 8948–8957.
[26] Y. Liu, W. Zhang, Y. Cao, Y. Liu, S. Bergmeier, X. Chen, Small compound inhibitors of basal glucose transport inhibit cell proliferation and induce apoptosis in cancer cells via glucose-deprivation-like mechanisms, Cancer Lett. 298 (2010) 176–185. https://doi.org/10.1016/j.canlet.2010.07.002.
[27] T. Tuccinardi, C. Granchi, J. Iegre, I. Paterni, S. Bertini, M. Macchia, A. Martinelli, Y. Qian, X. Chen, F. Minutolo, Oxime-based inhibitors of glucose transporter 1 displaying antiproliferative effects in cancer cells, Bioorg. Med. Chem. Lett. 23 (2013) 6923–6927. https://doi.org/10.1016/j.bmcl.2013.09.037.
[28] D.A. Chan, P.D. Sutphin, P. Nguyen, S. Turcotte, E.W. Lai, A. Banh, G.E. Reynolds, J.-T. Chi, J. Wu, D.E. Solow-Cordero, M. Bonnet, J.U. Flanagan, D.M. Bouley, E.E. Graves, W.A. Denny, M.P. Hay, A.J. Giaccia, Targeting GLUT1 and the Warburg Effect in Renal Cell Carcinoma by Chemical Synthetic Lethality, Sci. Transl. Med. 3 (2011) 94ra70-94ra70. https://doi.org/10.1126/scitranslmed.3002394.
[29] C.-S. Chen, D. Wang, S.K. Kulp, Glucose transporter inhibitors, US9174951B2, 2015. https://patents.google.com/patent/US9174951B2/en (accessed May 5, 2020).
[30] Y. Meng, X. Xu, H. Luan, L. Li, W. Dai, Z. Li, J. Bian, The progress and development of GLUT1 inhibitors targeting cancer energy metabolism, Future Med. Chem. 11 (2019) 2333–2352. https://doi.org/10.4155/fmc-2019-0052.
[31] S. Prost, F. Relouzat, M. Spentchian, Y. Ouzegdouh, J. Saliba, G. Massonnet, J.-P. Beressi, E. Verhoeyen, V. Raggueneau, B. Maneglier, S. Castaigne, C. Chomienne, S. Chrétien, P. Rousselot, P. Leboulch, Erosion of the chronic myeloid leukaemia stem cell pool by PPARγ agonists, Nature. 525 (2015) 380–383. https://doi.org/10.1038/nature15248.
[32] V.G. Keshamouni, R.C. Reddy, D.A. Arenberg, B. Joel, V.J. Thannickal, G.P. Kalemkerian, T.J. Standiford, Peroxisome proliferator-activated receptor-γ activation inhibits tumor progression in non-small-cell lung cancer, Oncogene. 23 (2004) 100–108. https://doi.org/10.1038/sj.onc.1206885.
[33] H. Joshi, T. Pal, C. Ramaa, A new dawn for the use of thiazolidinediones in cancer therapy, Expert Opin. Investig. Drugs. 23 (2014) 501–510. https://doi.org/10.1517/13543784.2014.884708.
[34] P. Thaggikuppe Krishnamurthy, M. Joghee Nanjan Chandrasekar, M. Joghee Nanjan, Newer Approaches to the Discovery of Glitazones, Mini-Rev. Org. Chem. 10 (2013) 66–72. https://doi.org/10.2174/1570193X11310010005.
[35] S. Wei, S.K. Kulp, C.-S. Chen, Energy Restriction as an Antitumor Target of Thiazolidinediones, J. Biol. Chem. 285 (2010) 9780–9791. https://doi.org/10.1074/jbc.M109.065466.
[36] H.A. Omar, S.A. Salama, E.-S.A. Arafa, J.-R. Weng, Antitumor effects of energy restriction-mimetic agents: thiazolidinediones, Biol. Chem. 394 (2013) 865–870. https://doi.org/10.1515/hsz-2013-0139.

[37] E.A. Arafa, A.H. Abdelazeem, H.H. Arab, H.A. Omar, OSU-CG5, a novel energy restriction mimetic agent, targets human colorectal cancer cells in vitro, Acta Pharmacol. Sin. 35 (2014) 394–400. https://doi.org/10.1038/aps.2013.183.
[38] A. Gutierréz-Hernández, Y. Galván-Ciprés, E.A. Domínguez-Mendoza, Y. Aguirre-Vidal, S. Estrada-Soto, J.C. Almanza-Pérez, G. Navarrete-Vázquez, Design, Synthesis, Antihyperglycemic Studies, and Docking Simulations of Benzimidazole-Thiazolidinedione Hybrids, J. Chem. 2019 (2019) 1–8. https://doi.org/10.1155/2019/1650145.
[39] B. Colín-Lozano, S. Estrada-Soto, F. Chávez-Silva, A. Gutiérrez-Hernández, L. Cerón-Romero, A. Giacoman-Martínez, J. Almanza-Pérez, E. Hernández-Núñez, Z. Wang, X. Xie, M. Cappiello, F. Balestri, U. Mura, G. Navarrete-Vazquez, Design, Synthesis and in Combo Antidiabetic Bioevaluation of Multitarget Phenylpropanoic Acids, Molecules. 23 (2018) 340. https://doi.org/10.3390/molecules23020340.
[40] H. Joshi, K. Marulkar, V.G. and C.S. Ramaa*, Hydroxy Cinnamic Acid Derivatives as Partial PPARγ Agonists: In silico Studies, Synthesis and Biological Characterization Against Chronic Myeloid Leukemia Cell Line (K562), Anticancer Agents Med. Chem. (2017). http://www.eurekaselect.com/143017/article (accessed December 18, 2019).
[41] T. Pal, H. Joshi, C.S. Ramaa, Design and Development of Oxazol-5-Ones as Potential Partial PPAR-γ Agonist Against Cancer Cell Lines, Anticancer Agents Med. Chem. 14 (2014) 872–883. https://doi.org/10.2174/1871520614666140528155118.
[42] U. Bhanushali, S. Rajendran, K. Sarma, P. Kulkarni, K. Chatti, S. Chatterjee, C.S. Ramaa, 5-Benzylidene-2,4-thiazolidenedione derivatives: Design, synthesis and evaluation as inhibitors of angiogenesis targeting VEGR-2, Bioorganic Chem. 67 (2016) 139–147. https://doi.org/10.1016/j.bioorg.2016.06.006.
[43] K. Tilekar, N. Upadhyay, N. Jänsch, M. Schweipert, P. Mrowka, F.J. Meyer-Almes, C.S. Ramaa, Discovery of 5-Naphthylidene-2,4-thiazolidinedione derivatives as selective HDAC8 inhibitors and evaluation of their cytotoxic effects in leukemic cell lines, Bioorganic Chem. (2019) 103522. https://doi.org/10.1016/j.bioorg.2019.103522.
[44] R. Mohan, A.K. Sharma, S. Gupta, C.S. Ramaa, Design, synthesis, and biological evaluation of novel 2,4-thiazolidinedione derivatives as histone deacetylase inhibitors targeting liver cancer cell line, Med. Chem. Res. 21 (2012) 1156–1165. https://doi.org/10.1007/s00044-011-9623-3.
[45] K. Kapoor, J.S. Finer-Moore, B.P. Pedersen, L. Caboni, A. Waight, R.C. Hillig, P. Bringmann, I. Heisler, T. Müller, H. Siebeneicher, R.M. Stroud, Mechanism of inhibition of human glucose transporter GLUT1 is conserved between cytochalasin B and phenylalanine amides, Proc. Natl. Acad. Sci. U. S. A. 113 (2016) 4711–4716. https://doi.org/10.1073/pnas.1603735113.
[46] V. Patil, K. Tilekar, S. Mehendale-Munj, R. Mohan, C.S. Ramaa, Synthesis and primary cytotoxicity evaluation of new 5-benzylidene-2,4-thiazolidinedione derivatives, Eur. J. Med. Chem. 45 (2010) 4539–4544. https://doi.org/10.1016/j.ejmech.2010.07.014.
[47] R. Wieczorke, S. Dlugai, S. Krampe, E. Boles, Characterisation of mammalian GLUT glucose transporters in a heterologous yeast expression system, Cell. Physiol. Biochem. Int. J. Exp. Cell. Physiol. Biochem. Pharmacol. 13 (2003) 123–134. https://doi.org/10.1159/000071863.
[48] M. Uldry, B. Thorens, The SLC2 family of facilitated hexose and polyol transporters, Pfl&#xfffd;gers Arch. Eur. J. Physiol. 447 (2004) 480–489. https://doi.org/10.1007/s00424-003-1085-0.
[49] N. Yan, A Glimpse of Membrane Transport through Structures—Advances in the Structural Biology of the GLUT Glucose Transporters, J. Mol. Biol. 429 (2017) 2710–2725. https://doi.org/10.1016/j.jmb.2017.07.009.
[50] M. Mueckler, W. Weng, M. Kruse, Glutamine 161 of Glut1 glucose transporter is critical for transport activity and exofacial ligand binding, J. Biol. Chem. 269 (1994) 20533–20538.

[51] A. Daina, O. Michielin, V. Zoete, iLOGP: a simple, robust, and efficient description of n-octanol/water partition coefficient for drug design using the GB/SA approach, J. Chem. Inf. Model. 54 (2014) 3284–3301. https://doi.org/10.1021/ci500467k.
[52] A. Daina, O. Michielin, V. Zoete, SwissADME: a free web tool to evaluate pharmacokinetics, drug-likeness and medicinal chemistry friendliness of small molecules, Sci. Rep. 7 (2017) 42717. https://doi.org/10.1038/srep42717.
[53] M.L. Amin, P-glycoprotein Inhibition for Optimal Drug Delivery, Drug Target Insights. 7 (2013) 27–34. https://doi.org/10.4137/DTI.S12519.
[54] C.A. Lipinski, F. Lombardo, B.W. Dominy, P.J. Feeney, Experimental and computational approaches to estimate solubility and permeability in drug discovery and development settings, Adv. Drug Deliv. Rev. 46 (2001) 3–26. https://doi.org/10.1016/s0169-409x(00)00129-0.
[55] D.F. Veber, S.R. Johnson, H.-Y. Cheng, B.R. Smith, K.W. Ward, K.D. Kopple, Molecular properties that influence the oral bioavailability of drug candidates, J. Med. Chem. 45 (2002) 2615–2623. https://doi.org/10.1021/jm020017n.
[56] A.K. Ghose, V.N. Viswanadhan, J.J. Wendoloski, A Knowledge-Based Approach in Designing Combinatorial or Medicinal Chemistry Libraries for Drug Discovery. 1. A Qualitative and Quantitative Characterization of Known Drug Databases, J. Comb. Chem. 1 (1999) 55–68. https://doi.org/10.1021/cc9800071.
[57] W.J. Egan, K.M. Merz,, J.J. Baldwin, Prediction of Drug Absorption Using Multivariate Statistics, J. Med. Chem. 43 (2000) 3867–3877. https://doi.org/10.1021/jm000292e.
[58] I. Muegge, S.L. Heald, D. Brittelli, Simple selection criteria for drug-like chemical matter, J. Med. Chem. 44 (2001) 1841–1846. https://doi.org/10.1021/jm015507e.
[59] C. LEMA, A. VARELA-RAMIREZ, R.J. AGUILERA, Differential nuclear staining assay for high-throughput screening to identify cytotoxic compounds, Curr. Cell. Biochem. 1 (2011) 1–14.
[60] Y. Ren, C. Yuan, Y. Qian, H.-B. Chai, X. Chen, M. Goetz, A.D. Kinghorn, Constituents of an extract of Cryptocarya rubra housed in a repository with cytotoxic and glucose transport inhibitory effects, J. Nat. Prod. 77 (2014) 550–556. https://doi.org/10.1021/np400809w.
[61] Y. Liu, Y. Cao, W. Zhang, S. Bergmeier, Y. Qian, H. Akbar, R. Colvin, J. Ding, L. Tong, S. Wu, J. Hines, X. Chen, A small-molecule inhibitor of glucose transporter 1 downregulates glycolysis, induces cell-cycle arrest, and inhibits cancer cell growth in vitro and in vivo, Mol. Cancer Ther. 11 (2012) 1672–1682. https://doi.org/10.1158/1535-7163.MCT-12-0131.
[62] D.A. Gutierrez, R.E. DeJesus, L. Contreras, I.A. Rodriguez-Palomares, P.J. Villanueva, K.S. Balderrama, L. Monterroza, M. Larragoity, A. Varela-Ramirez, R.J. Aguilera, A new pyridazinone exhibits potent cytotoxicity on human cancer cells via apoptosis and poly-ubiquitinated protein accumulation, Cell Biol. Toxicol. 35 (2019) 503–519. https://doi.org/10.1007/s10565-019-09466-8.
[63] A.V. Orang, J. Petersen, R.A. McKinnon, M.Z. Michael, Micromanaging aerobic respiration and glycolysis in cancer cells, Mol. Metab. 23 (2019) 98–126. https://doi.org/10.1016/j.molmet.2019.01.014.
[64] E. Świderska, J. Strycharz, A. Wróblewski, J. Szemraj, J. Drzewoski, A. Śliwińska, Role of PI3K/AKT Pathway in Insulin-Mediated Glucose Uptake, in: L. Szablewski (Ed.), Blood Glucose Levels, IntechOpen, 2020. https://doi.org/10.5772/intechopen.80402.
[65] Y. Xie, X. Shi, K. Sheng, G. Han, W. Li, Q. Zhao, B. Jiang, J. Feng, J. Li, Y. Gu, PI3K/Akt signaling transduction pathway, erythropoiesis and glycolysis in hypoxia, Mol. Med. Rep. 19 (2019) 783–791. https://doi.org/10.3892/mmr.2018.9713.
[66] Y. Wang, J. Shen, N. Arenzana, W. Tirasophon, R.J. Kaufman, R. Prywes, Activation of ATF6 and an ATF6 DNA binding site by the endoplasmic reticulum stress response, J. Biol. Chem. 275 (2000) 27013–27020. https://doi.org/10.1074/jbc.M003322200.

[67] R. Bremner, E. Zacksenhaus, Cyclins, Cdks, E2f, Skp2, and More at the First International RB Tumor Suppressor Meeting, Cancer Res. 70 (2010) 6114–6118. https://doi.org/10.1158/0008-5472.CAN-10-0358.
[68] C. Giacinti, A. Giordano, RB and cell cycle progression, Oncogene. 25 (2006) 5220–5227. https://doi.org/10.1038/sj.onc.1209615.
[69] R. Iwakawa, T. Kohno, Y. Anami, M. Noguchi, K. Suzuki, Y. Matsuno, K. Mishima, R. Nishikawa, F. Tashiro, J. Yokota, Association of p16 homozygous deletions with clinicopathologic characteristics and EGFR/KRAS/p53 mutations in lung adenocarcinoma, Clin. Cancer Res. Off. J. Am. Assoc. Cancer Res. 14 (2008) 3746–3753. https://doi.org/10.1158/1078-0432.CCR-07-4552.
[70] Y. Li, F. Dida, A. Iwao, T. Deguchi, E. Azuma, Y. Komada, Cell cycle dependency of caspase activation in Fas-induced apoptosis in leukemia cells, Cancer Sci. 98 (2007) 1174–1183. https://doi.org/10.1111/j.1349-7006.2007.00523.x.
[71] A. Kabir, K. Tilekar, N. Upadhyay, C.S. Ramaa, Novel Anthraquinone Derivatives as Dual Inhibitors of Topoisomerase 2 and Casein Kinase 2: In Silico Studies, Synthesis and Biological Evaluation on Leukemic Cell Lines, Anticancer Agents Med. Chem. 18 (2019) 1551–1562. https://doi.org/10.2174/1871520618666180423111309.
[72] J. Tripp, C. Essl, C.V. Iancu, E. Boles, J.-Y. Choe, M. Oreb, Establishing a yeast-based screening system for discovery of human GLUT5 inhibitors and activators, Sci. Rep. 7 (2017) 6197. https://doi.org/10.1038/s41598-017-06262-4.
[73] T. Kasahara, M. Kasahara, Characterization of rat Glut4 glucose transporter expressed in the yeast Saccharomyces cerevisiae: comparison with Glut1 glucose transporter, Biochim. Biophys. Acta. 1324 (1997) 111–119. https://doi.org/10.1016/s0005-2736(96)00217-9.
[74] A.M. George Thompson, O. Ursu, P. Babkin, C.V. Iancu, A. Whang, T.I. Oprea, J. Choe, Discovery of a specific inhibitor of human GLUT5 by virtual screening and in vitro transport evaluation, Sci. Rep. 6 (2016) 24240. https://doi.org/10.1038/srep24240.
[75] M.R. Peram, S. Jalalpure, V. Kumbar, S. Patil, S. Joshi, K. Bhat, P. Diwan, Factorial design based curcumin ethosomal nanocarriers for the skin cancer delivery: *in vitro* evaluation, J. Liposome Res. 29 (2019) 291–311. https://doi.org/10.1080/08982104.2018.1556292.
[76] M.R. Peram, S. Jalalpure, V. Kumbar, S. Patil, S. Joshi, K. Bhat, P. Diwan, Factorial design based curcumin ethosomal nanocarriers for the skin cancer delivery: *in vitro* evaluation, J. Liposome Res. 29 (2019) 291–311. https://doi.org/10.1080/08982104.2018.1556292.
[77] N. Jänsch, C. Meyners, M. Muth, A. Kopranovic, O. Witt, I. Oehme, F.-J. Meyer-Almes, The enzyme activity of histone deacetylase 8 is modulated by a redox-switch, Redox Biol. 20 (2019) 60–67. https://doi.org/10.1016/j.redox.2018.09.013.
[78] A. Volund, Application of the Four-Parameter Logistic Model to Bioassay: Comparison with Slope Ratio and Parallel Line Models, Biometrics. 34 (1978) 357. https://doi.org/10.2307/2530598.

Acknowledgements. This study was supported by Indo-Poland joint research program grant from Department of Science and Technology (DST) with reference number DST/INT/Pol/P-27/2016 (to CSR), the United State NIH R01GM123103 (to JC) and NIMHD grant 5U54MD007592 to the Border Biomedical Research Center (BBRC) at UTEP (to RA). We thank Gavin Black (undergraduate student at North Carolina State University), Dawson Wright and Garrett Wood (undergraduate students at East Carolina University), Valerie Riehl and Andrea Adam (at Rosalind Franklin University of Medicine and Science) for technical assistance.

Competing Interests. The authors declare no competing interests.

Author Contributions. KT and CSR conceived the idea and designed the molecules. KT and NU synthesized and characterized compounds. JC and CVI performed the GLUT assays and ligand docking. F-JM Undertook the HDAC studies. KT Compiled the data and drafted the manuscript. RA designed and JDH, LHM and PM performed cytotoxicity, apoptosis and cell cycle analysis. CSR, JC, RA and F-JM supervised the project, formulated the data including figures and tables, and wrote the manuscript. All authors contributed to the discussion of the results and preparation of the manuscript.

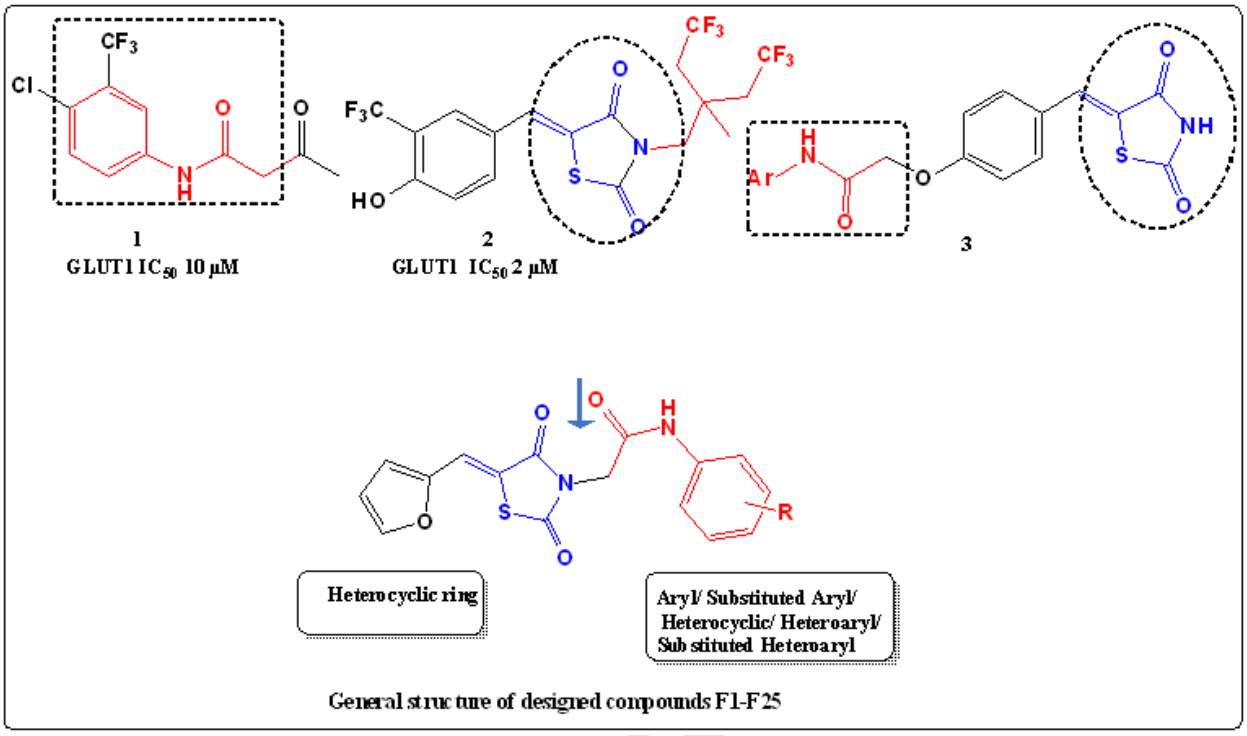

General structure of designed compounds F1-F25

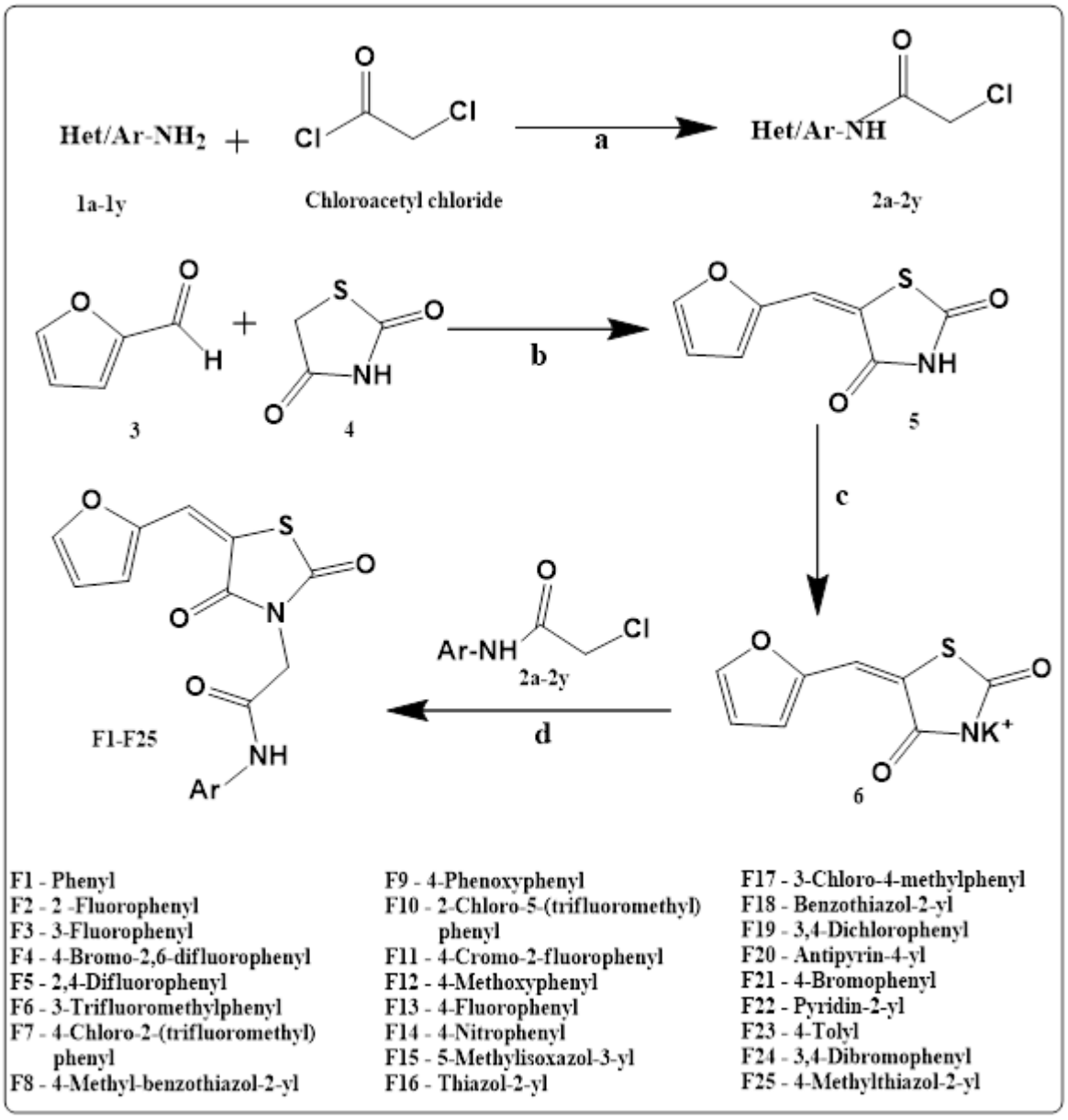

F1 - Phenyl
F2 - 2 -Fluorophenyl
F3 - 3-Fluorophenyl
F4 - 4-Bromo-2,6-difluorophenyl
F5 - 2,4-Difluorophenyl
F6 - 3-Trifluoromethylphenyl
F7 - 4-Chloro-2-(trifluoromethyl) phenyl
F8 - 4-Methyl-benzothiazol-2-yl
F9 - 4-Phenoxyphenyl
F10 - 2-Chloro-5-(trifluoromethyl) phenyl
F11 - 4-Cromo-2-fluorophenyl
F12 - 4-Methoxyphenyl
F13 - 4-Fluorophenyl
F14 - 4-Nitrophenyl
F15 - 5-Methylisoxazol-3-yl
F16 - Thiazol-2-yl
F17 - 3-Chloro-4-methylphenyl
F18 - Benzothiazol-2-yl
F19 - 3,4-Dichlorophenyl
F20 - Antipyrin-4-yl
F21 - 4-Bromophenyl
F22 - Pyridin-2-yl
F23 - 4-Tolyl
F24 - 3,4-Dibromophenyl
F25 - 4-Methylthiazol-2-yl

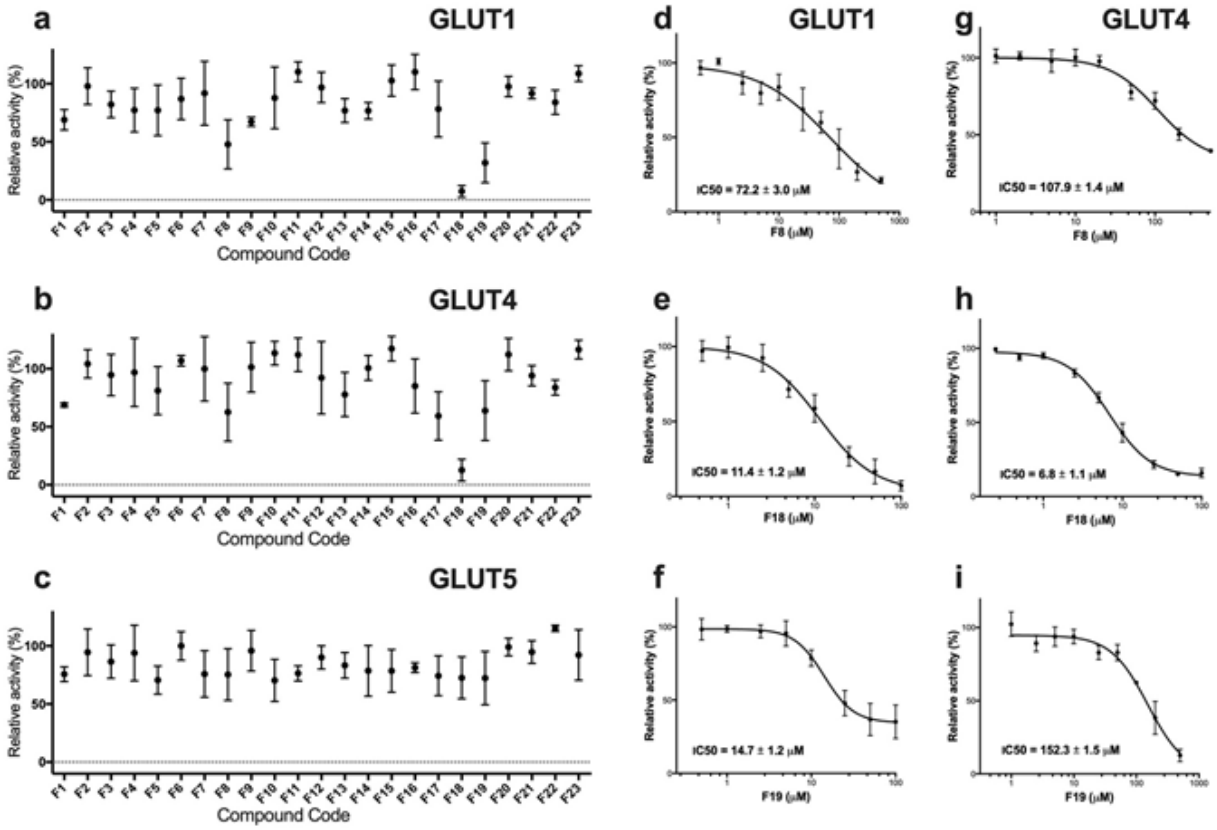
a
GLUT1
Relative activity (%)
Compound Code
b
GLUT4
c
GLUT5
d
GLUT1
IC50 = 72.2 ± 3.0 μM
F8 (μM)
e
IC50 = 11.4 ± 1.2 μM
F18 (μM)
f
IC50 = 14.7 ± 1.2 μM
F19 (μM)
g
GLUT4
IC50 = 107.9 ± 1.4 μM
F8 (μM)
h
IC50 = 6.8 ± 1.1 μM
F18 (μM)
i
IC50 = 152.3 ± 1.5 μM
F19 (μM)

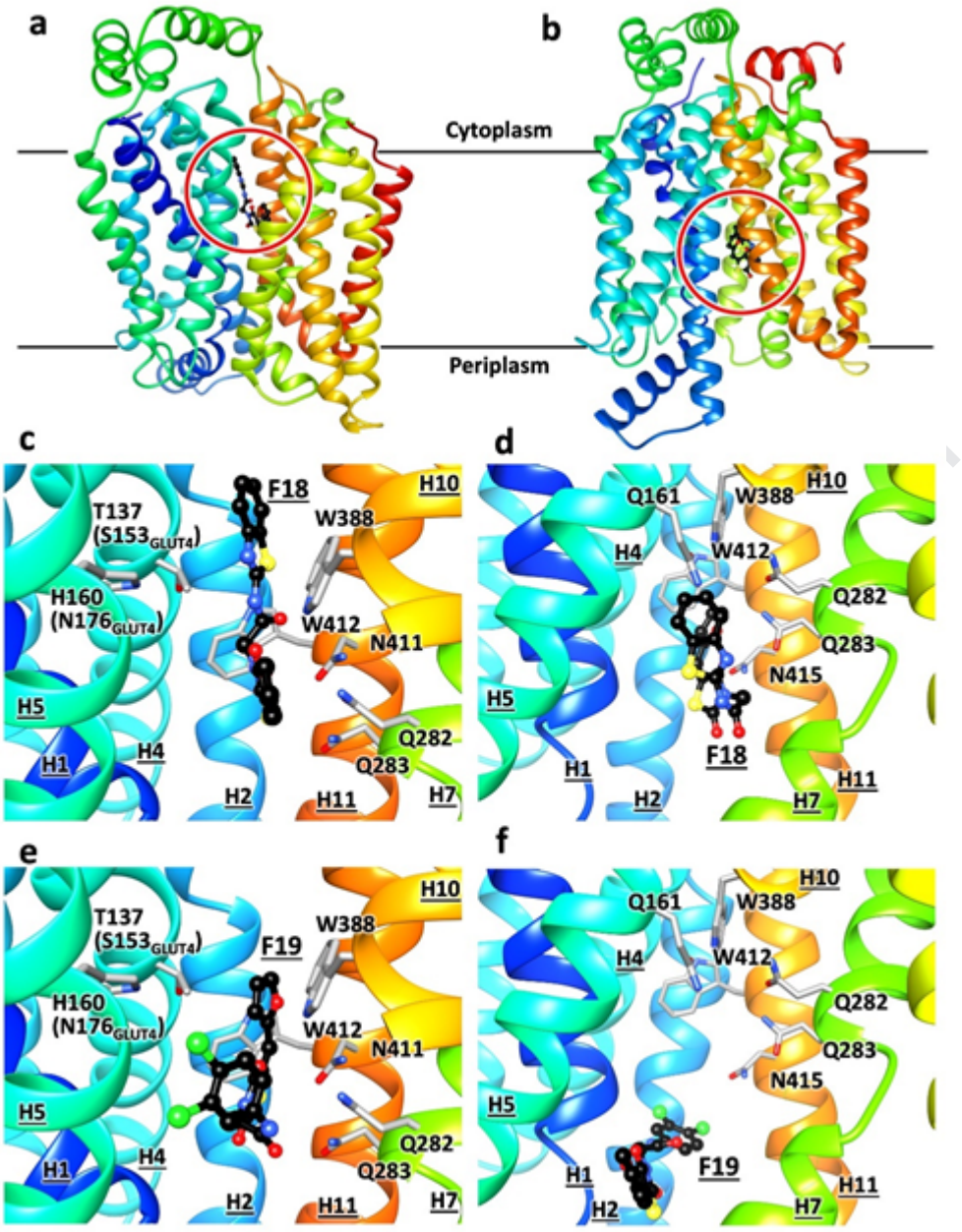
a
b
Cytoplasm
Periplasm
c
T137
(S153GLUT4)
H160
(N176GLUT4)
F18
H10
W388
W412
N411
Q282
Q283
H5
H1
H4
H2
H11
H7
d
Q161
W388
H10
H4
W412
Q282
Q283
N415
H5
F18
H1
H2
H11
H7
e
T137
(S153GLUT4)
H160
(N176GLUT4)
F19
H10
W388
W412
N411
Q282
Q283
H5
H1
H4
H2
H11
H7
f
Q161
W388
H10
H4
W412
Q282
Q283
N415
H5
H1
F19
H2
H11
H7

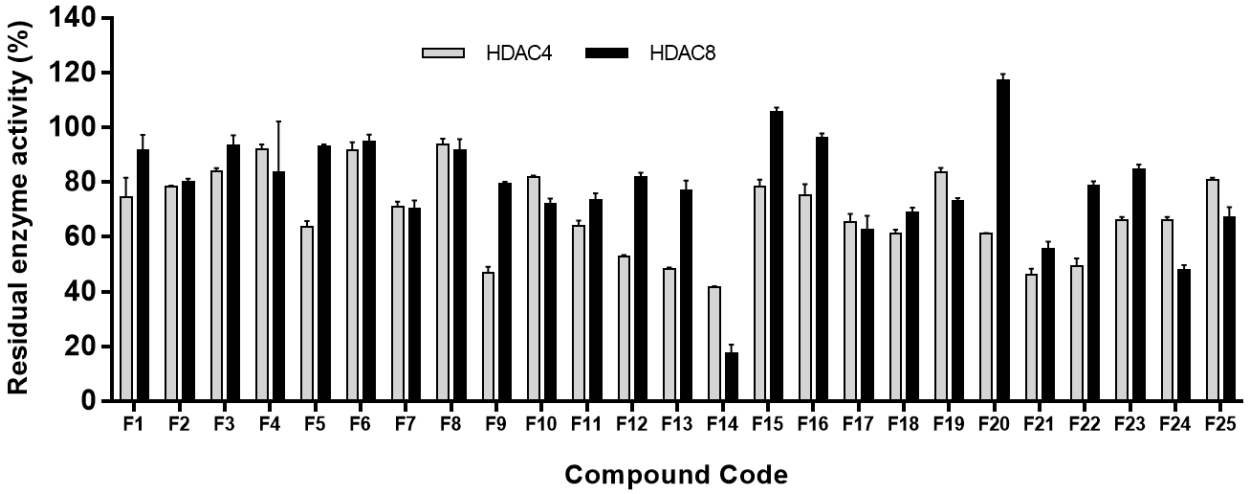

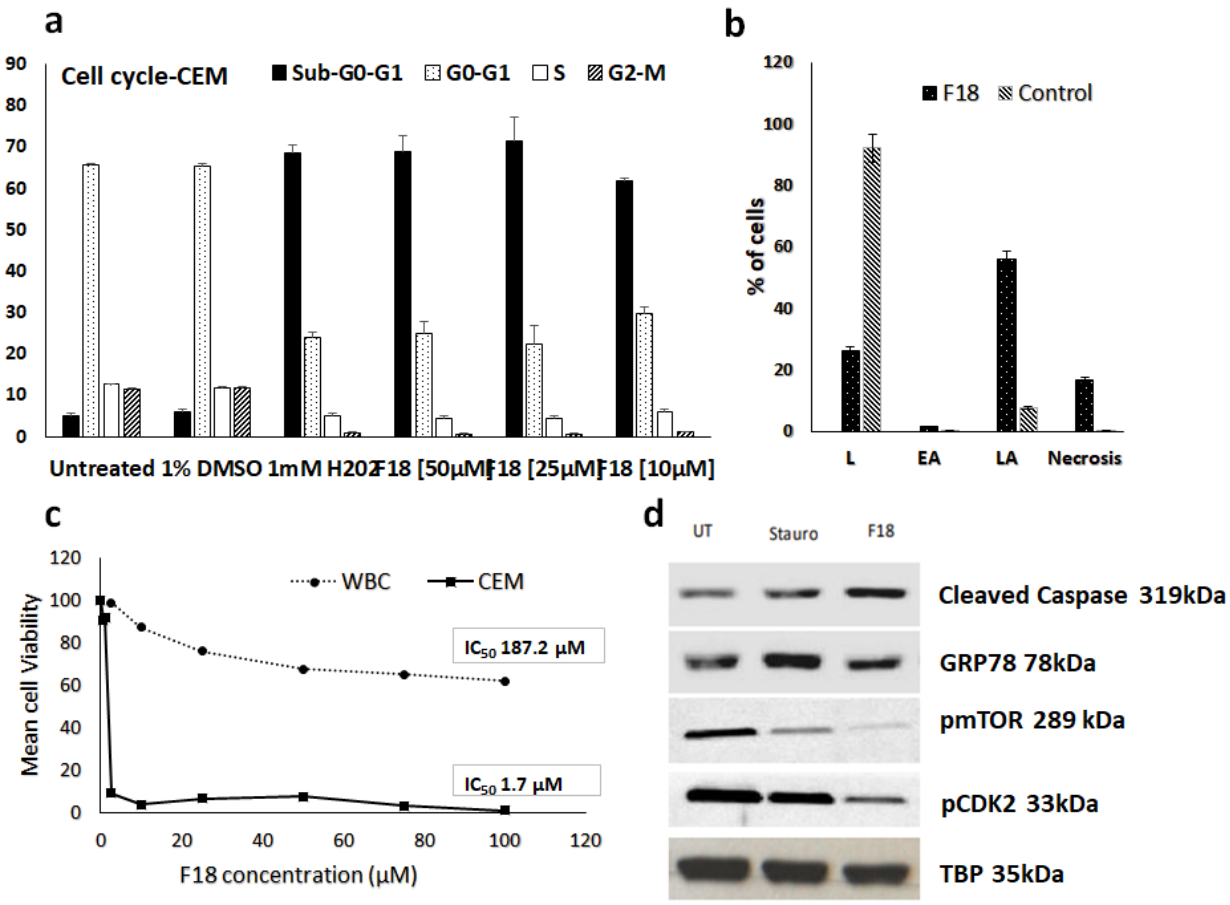
a
Cell cycle-CEM
Sub-G0-G1
G0-G1
S
G2-M
90
80
70
60
50
40
30
20
10
0
Untreated
1% DMSO
1mM H202
F18 [50µM]
F18 [25µM]
F18 [10µM]
b
F18
Control
% of cells
120
100
80
60
40
20
0
L
EA
LA
Necrosis
c
WBC
CEM
Mean cell Viability
IC50 187.2 µM
IC50 1.7 µM
F18 concentration (µM)
d
UT
Stauro
F18
Cleaved Caspase 319kDa
GRP78 78kDa
pmTOR 289 kDa
pCDK2 33kDa
TBP 35kDa

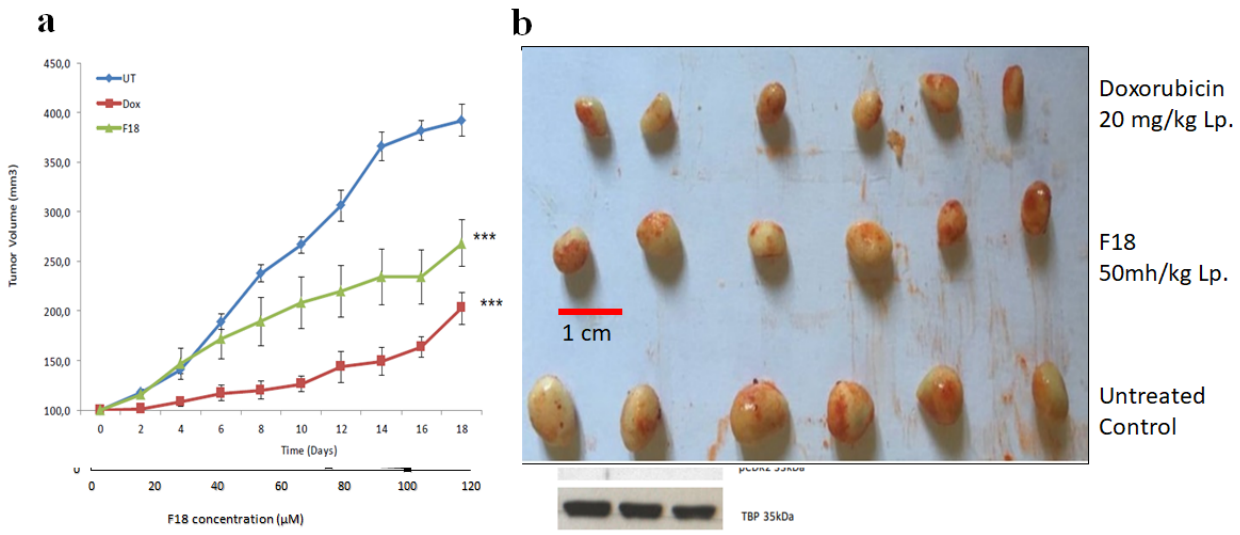

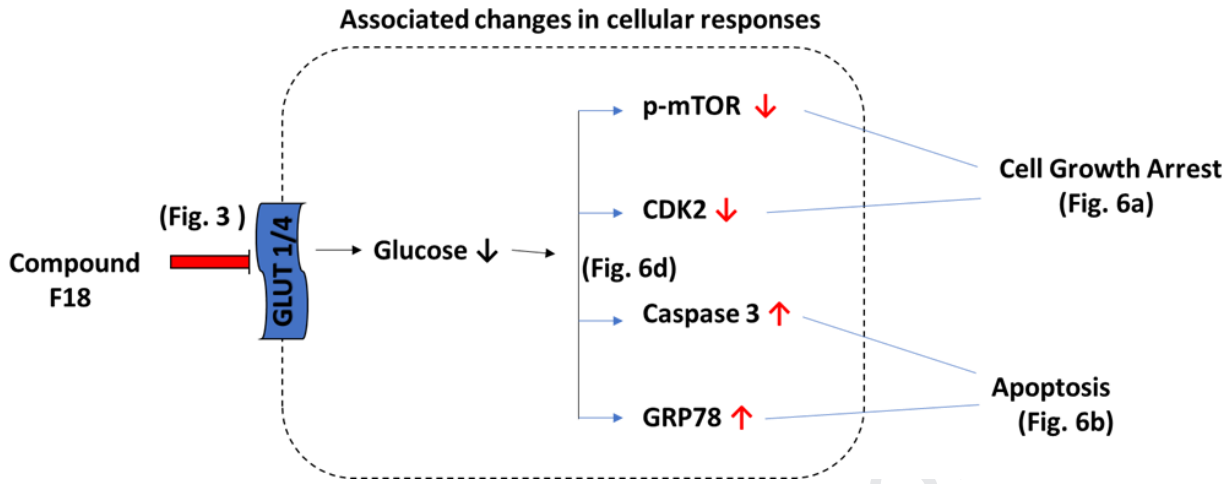

- A series of novel furyl thiazolidinedione derivatives were designed and synthesized as GLUT1 inhibitors.
- The representative Compound F18 demonstrated GLUT1 and GLUT4 inhibitory activity and potent antiproliferative activity against CEM cells.
- Compound F18 could block the cell cycle in the sub G0/G1 phase and induce apoptosis.
- Western blotting analysis of F18 caused decreased in expression levels of p-mTOR and CDK2 proteins, induced Caspase 3 activation and GRP78 upregulation.
- Compound F18 exhibited promising in vivo antitumor activity in the CEM xenograft model.

Declaration of interests

☒ The authors declare that they have no known competing financial interests or personal relationships that could have appeared to influence the work reported in this paper.

☐The authors declare the following financial interests/personal relationships which may be considered as potential competing interests: